Dynamical structures of internally heated thermal convection with temperature-dependent viscosity

Hisashi Okuda
Research Institute for Mathematical Sciences, Kyoto University

October 10, 2025

Abstract

Thermal convection of fluids with temperature-dependent viscosity is of particular interest in understanding mantle convection in terrestrial planets. Dynamical structures of convection with temperature-dependent viscosity driven by bottom heating have been extensively investigated, revealing characteristics relevant to geodynamics such as mobile, sluggish lid, and stagnant lid regimes. While internal heating is recognized as a significant heat source driving mantle convection, its influence on convective structures and transitions among regimes remains less understood.

We study the dynamical regimes of internally heated thermal convection with temperature-dependent viscosity. The viscosity is given by an exponential function of temperature. Two-dimensional steady-state convective solutions are obtained using the Newton method across a range of the Rayleigh numbers and the strengths of the temperature dependence of viscosity.

By classifying the steady solutions according to the top surface mobility, the sluggish lid regime is identified between the mobile and stagnant lid regimes with an intermediate range of the mobility. The solutions of the sluggish lid regime are characterized by a large viscosity contrast across the convective region and a steep increase in the height of the convective region with respect to the Rayleigh number. This feature likely reflects a transition in the effective boundary condition at the top of the convective region, from the stress-free condition for the mobile regime to the rigid condition for the stagnant lid regime.

The regime classification in this study is consistent with the difference in the scaling relations of each regime. The solutions of the mobile and stagnant lid regimes follow power-law functions of the Nusselt number with respect to the Rayleigh number, whose exponent is $1/4$ for low Rayleigh number cases, and $1/6$ for high Rayleigh number cases. The exponent $1/6$ can be theoretically derived by taking into account the effect of strong, narrow downward plumes in the steady convection cells.

Stability of representative steady solutions is evaluated by time integration calculations. In the unstable steady solutions, additional downward plumes grow from the boundary layer and are transported by the background convective flow. The stability is explained theoretically by comparing two timescales: the timescale of the Rayleigh–Taylor instability for the thermal boundary layer between the lid and the convective core, and that of horizontal entrainment by the background flow.

In addition, steady convective solutions with Arrhenius-law viscosity are calculated for several values of the parameters. The resulting regime diagrams qualitatively agree with that for convection with the exponential temperature-dependent viscosity. There are slight shifts in locations of the regime boundaries, which may depend on the absolute temperature.

This study provides fundamental insights into the fluid dynamics underlying the diversity of structures and their transitions in thermal convection with temperature-dependent viscosity. The regime classification obtained through this study will help to understand the interior structures of various solar and extrasolar planets.

Contents

Chapter 1

Introduction

1.1 Geophysical background — Mantle convection in terrestrial planets

Thermal convection is a fundamental problem that plays a pivotal role in the thermal and dynamical states of the interiors of the Earth and other terrestrial planets (e.g. Schubert et al., 2001; Turcotte and Schubert, 2014; Ribe, 2018). It leads to efficient spatial heat transport and material movement in a horizontal fluid layer. When a fluid layer is heated from below or within, and cooled from above, the diffusive temperature gradient can cause a buoyancy-driven instability, whereby hot, buoyant fluid rises and cold, denser fluid sinks. This mechanism gives rise to circulating fluid motion enhancing heat transport by advection, in contrast to hydrostatic thermal conduction (Chandrasekhar, 1961). The onset of convection is demonstrated by a dimensionless parameter, known as the Rayleigh number, which describes the strength of buoyancy relative to the viscous force scale. When the Rayleigh number exceeds a critical threshold, the conductive state becomes unstable and buoyant plumes begin to develop. Once instability occurs, circular convective flow is formed resulting in stationary convection cells with characteristic thermal and dynamical patterns (e.g. Bénard, 1900). The Rayleigh number still governs the intensity of finite-amplitude convection, which is related to the pattern formation. When the Rayleigh number increases further, the cellular pattern becomes unstable and time-dependent patterns come to emerge (e.g. Busse, 1967a,b). This can be interpreted as manifestations of stable steady solutions of the nonlinear partial differential equations that govern fluid dynamics and heat transport.

The interiors of terrestrial planets like the Earth are generally in a convectively unstable state. They have substantial heat sources inside themselves due to radioactive decay, cooling from the surface (secular cooling), and, in some cases, residual heat from planetary accretion or core formation (Jaupart et al., 2015). The mantle is a solid layer between the planetary core and the crust, and it is heated from the bottom and within itself, and cooled from the top. Estimates of the Rayleigh number based on the Earth's parameters, for example, suggest that it greatly exceeds the critical value required for the onset of convection (Schubert et al., 2001). Since the mantle is the outermost solid layer in which thermal convection occurs, mantle convection should influence heat transport and surface dynamics in terrestrial planetary bodies.

Mantle convection exerts a profound influence on various geophysical processes at the planetary scale. McKenzie et al. (1974) performed numerical experiments of thermal convection to illustrate the thermal and dynamical states that are related to geophysical observations both qualitatively and quantitatively. Convective flow is closely coupled with surface tectonic activities, such as plate motion, crustal deformation, and the formation and evolution of topography (e.g. Tackley, 2000). Thus surface tectonics is associated with the underlying mantle convection patterns, and both of them are characterized by the same set of planetary properties. The intensity of convection is also linked to the total heat transport from the core to the surface. Scaling laws of heat transport as functions of planetary properties are useful for providing quantitative estimates of planetary cooling processes (e.g. Thiriet et al., 2019). Furthermore, mantle dynamics can indirectly influence planetary climate and the generation of the intrinsic magnetic fields through interactions with the atmosphere and the core (Foley and Driscoll, 2016). Therefore, understanding the thermal and dynamical characteristics of mantle convection is essential for exploring the environment and thermal evolution of planets.

In this context, theoretical studies of mantle convection provide a framework for understanding geophysical phenomena and long-term evolution of terrestrial planets. By analyzing mathematical models of mantle convection, we can extract general insights that are applicable to a wide range of planetary conditions and properties. Such an approach is essential for identifying key parameters to establish a predictive foundation for planetary sciences.

1.2 Mathematical modeling of mantle convection

Mathematical modeling of mantle convection based on physical governing equations is essential for the analyses of the dynamics. The primitive model of mantle convection has been established as the Rayleigh–Bénard convection with the infinite

Prandtl number (e.g. Schubert et al., 2001). In this model, the inertia term is negligible in the equation of motion, since the mantle materials can be considered to be a highly viscous continuous medium in which momentum diffusivity is about 10^{23} times larger than thermal diffusivity. Mantle convection models have been developed based on this model, incorporating characteristics specific to the mantle materials.

One of the typical features of mantle convection models is strong spatial variation in viscosity. Studies of mantle rheology have shown that mantle viscosity depends on temperature, pressure, and composition, and it can vary by several orders of magnitude across the mantle (Ricard, 2015). The viscosity variation significantly influences the pattern formation in thermal convection. In particular, temperature has the most significant effect on the viscosity variation in the mantle. Based on the microscopic properties of mantle materials, viscosity η is modeled by the Arrhenius law, given by the following (dimensionless) function of temperature T (e.g. Grigné, 2023):

$$\eta(T) \propto \exp\left(\frac{E_a}{T+T_o}\right), \tag{1.1}$$

where E_a is the activation energy normalized by the universal gas constant and a characteristic temperature scale of the system, and T_o is a reference value of absolute temperature. The viscosity variation is primarily controlled by E_a, while T_o accounts for the absolute temperature and does not directly affect the viscosity variation. When we parameterize the viscosity variation by temperature, a simplified rheology model called the Frank-Kamenetskii approximation has been commonly employed so far (e.g. Christensen, 1984):

$$\eta(T) \propto \exp\left(-\gamma T\right). \tag{1.2}$$

The parameter γ, called the Frank-Kamenetskii parameter, describes the temperature dependence in this equation. Different convection patterns have been observed in numerical simulations using various values of E_a or γ (e.g. Moresi and Solomatov, 1995).

Another essential effect to be included in mantle convection models is the presence of internal heat sources. While classical Rayleigh-Bénard convection considers a configuration with heating from below, the mantle of terrestrial planets is actually heated both from below and within. In fact, heat production in the Earth's mantle is estimated to be larger than heat supplied from the core (Jaupart et al., 2015), and many other terrestrial planets, satellites, and exoplanets may also have internal heat sources (Jain and Solomatov, 2022). While bottom heating induces strong upwelling columnar flow (plumes) originating from the thermal boundary layer along the bottom boundary, internal heating distributes thermal buoyancy throughout the mantle, often resulting in more diffuse upwelling flow rather than columnar plumes. The mode of heating can significantly influence patterns of convective flow and heat transport (e.g. Parmentier et al., 1994; Sotin and Labrosse, 1999; Parmentier and Sotin, 2000).

For the purpose of revealing fundamental properties of thermal convection with the features described above, some practical assumptions have been introduced in the modeling of Earth-like mantle convection. Incompressibility and the Boussinesq approximation are usually employed, under which density variation is neglected except for buoyancy caused by thermal expansion (Chandrasekhar, 1961). In addition, modeling often assumes that thermophysical properties are constant except for viscosity. Although these assumptions do not always hold for planets with extreme conditions such as exoplanets (e.g. Kameyama, 2025), they are considered reasonable for capturing fundamental behaviors of Earth-like planets. In the following sections, we will focus on the two types of features specialized for the mantle: temperature-dependent viscosity and internal heating.

1.3 Convection with temperature-dependent viscosity

Thermal convection models with temperature-dependent viscosity have been investigated mainly with the bottom heating condition, which is an extension of the classical Rayleigh–Bénard problem (e.g. Christensen, 1984). The temperature dependence, described by eqs. (1.1) or (1.2), generally causes the separation of a cold, highly viscous upper region and a hot, less viscous lower region within a fluid layer. As a result of this viscosity contrast in the vertical direction, the highly viscous upper layer becomes stiff and thermally conductive, while the lower layer maintains vigorous convection. By interpreting the conductive lid as the lithosphere (the upper rigid layer of the mantle) and the convective sublayer as the asthenosphere (the lower, relatively soft layer), we recognize temperature-dependent viscosity as an important property for mantle convection in terrestrial planets.

Dynamical structures of this system are characterized by the viscosity contrast across the fluid layer. The linear stability analysis (Stengel et al., 1982), the boundary layer analyses (e.g. Morris and Canright, 1984; Fowler, 1985), and the scaling analyses of finite-amplitude solutions (e.g. Solomatov, 1995; Moresi and Solomatov, 1995) have been performed so far. Solomatov (1995) succeeded in classifying the structures into three regimes depending on the viscosity contrast. When the

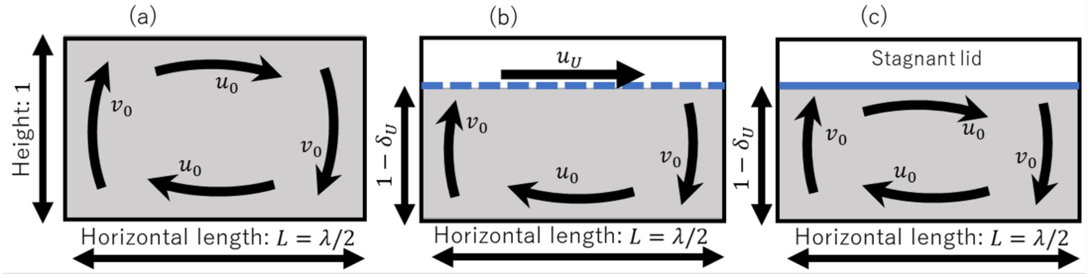

Figure 1.1: Schematic illustrations of a convection cell for three dynamical regimes. Convective region and conductive lids are indicated by grey shading and no-shading, respectively, for (a) mobile, (b) sluggish lid, and (c) stagnant lid regime convection. Adapted from Okuda and Takehiro (2023), licensed under CC BY 4.0.

viscosity contrast is small, convection occurs in the whole layer as in the case of constant viscosity (Small viscosity contrast regime, or Mobile regime). When viscosity contrast is large, a conductive lid is formed just below the top surface that is not involved in the convection (Stagnant lid regime). In addition, there is an intermediate regime with moderate viscosity contrast (Transitional regime or Sluggish lid regime), in which the conductive lid exists and drifts horizontally because the lid is not viscous enough to become stagnant. Figure 1.1 shows schematic illustrations of convective structures of each regime by Okuda and Takehiro (2023). As viscosity contrast increases from the left panel to the right, a conductive lid gradually emerges above the convective region, which drifts more slowly than convective flow. When viscosity contrast increases further, the lid becomes immobile.

Convective regimes can be distinguished in the parameter space to diagnose convective structures by the parameters. Solomatov (1995) presented a regime diagram on the parameter set of the Rayleigh number and viscosity contrast. The division of three regimes strongly depends on the viscosity contrast rather than on the Rayleigh number. Kameyama and Ogawa (2000) showed a regime diagram based on numerical solutions with horizontally wide boxes, in which the regime division is mostly independent of the Rayleigh number.

Reflecting the transitions of regimes, the scaling behaviors of key quantities such as lid thickness, interior temperature, and heat transport are expected to change as functions of input parameters. Solomatov (1995) derived scaling relations for each regime based on the conservation laws of energy and momentum. The presence or absence of a stagnant or sluggish lid changes the height of the convective region. This leads to different scaling functions for the output variables depending on the input parameters such as the temperature dependence of viscosity or the Rayleigh number. Figure 1.2 shows an example of the scaling functions for dimensionless heat

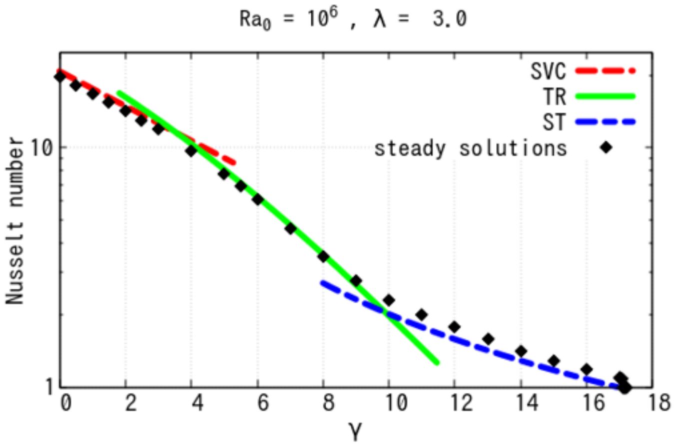

Figure 1.2: An example of the scaling function of heat transport to viscosity contrast for temperature-dependent viscosity convection driven by bottom heating (Okuda and Takehiro, 2023). Three curves show scaling functions of each regime (red: mobile, green: sluggish lid, blue: stagnant lid). The functions are derived theoretically and their arbitrary coefficients are obtained by fitting to numerical steady solutions shown by plots. Reproduced from Okuda and Takehiro (2023), licensed under CC BY 4.0.

transport (Nusselt number) to the strength of temperature dependence of viscosity proposed by Okuda and Takehiro (2023), in which Solomatov's scaling relations are extended to include the dependence on the horizontal wavelength for bottom-heated convection with temperature-dependent viscosity. The scaling functions are derived based on the momentum and energy conservations in each regime, and fitted to the steady-state solutions with different values of the wavelength. It is an interesting point from a mathematical point of view that different scaling relations arise even though heat transport and convective structures change gradually depending on the parameters.

1.4 Convection driven by internal heating

For iso-viscous fluids, internally heated convection has been studied as well as the bottom-heated convection. For convection of the iso-viscous fluid, Tritton and Zarraga (1967) and Roberts (1967) investigated the formation of convection cells in a purely internally heated fluid experimentally and theoretically. A scaling relation has been derived as a power-law function of the Rayleigh(–Roberts) number based on the boundary layer theory (e.g Parmentier et al., 1994; Turcotte and Schubert, 2014):

$$Nu \sim Ra^{1/4}, \tag{1.3}$$

where Nu is the Nusselt number, which is the dimensionless heat flux at the top surface, and Ra is the Rayleigh number. This scaling relation is in contrast to that of the bottom-heated convection, which gives $Nu \sim Ra^{1/3}$. Eq. (1.3) was derived assuming the typical configuration of internally heated convection in which convection with prominent downward plumes is the primary mode. The same exponent to Ra in the scaling function was obtained by numerical simulations in spherical shells (Deschamps et al., 2012), who included a factor that depends on the radius ratio of the shells. McKenzie et al. (1974) reported a slightly lower exponent than 1/4 by numerical calculations in two-dimensional boxes with aspect ratios of 1 (square) and 2.

In contrast, studies of internally heated convection of temperature-dependent viscous fluids have been less extensive than that of bottom-heated convection. Davaille and Jaupart (1993) conducted laboratory experiments of convection driven by cooling from above and no heating from below or within. This configuration is analogous to the internally heated convection system. They observed convection in the stagnant lid regime, and found that the viscosity contrast between the base of the stagnant lid and the isothermal core of convection becomes nearly constant. They suggested that this feature is a characteristic of the stagnant lid regime for the internally heated problem. Based on this result, the scaling functions for the stagnant lid regime have been proposed by numerical simulations in two-dimensional Cartesian boxes (e.g. Solomatov and Moresi, 2000) and three-dimensional spherical shells (e.g. Reese et al., 1999, 2005; Hüttig and Breuer, 2011).

The convective regimes for internally heated convection have been studied to some extent. Grasset and Parmentier (1998) performed numerical simulations in a two-dimensional Cartesian box with an aspect ratio of 2, and identified convective solutions of the no-lid regime and the conductive-lid regime, corresponding to the previously described mobile and stagnant lid regimes, respectively. The characteristics of convective structures of both regimes are basically consistent with those of bottom-heated convection, except for the absence of a thermal boundary layer along the bottom surface due to the insulating boundary condition. Grasset and Parmentier (1998) also found that scaling functions of the Nusselt number agree with that of the iso-viscous case (eq. 1.3) for both regimes by incorporating the viscosity contrast into the coefficients and rescaling to the effective values for the convective layer below the conductive lid. Choblet and Sotin (2000) described these two regimes by three-dimensional numerical calculations and examined regime transitions during cooling history of planets.

However, the regime classification of the structures of internally heated convection remains incomplete compared to the cases of bottom-heated convection. The regime diagram for internally heated convection also remains incomplete. In particular, the sluggish lid regime between the mobile and stagnant lid regimes has not been fully identified. Hüttig and Breuer (2011) performed numerical experiments for convection in spherical shells, and reported an intermediate regime that was characterized by the formation of horizontally elongated convection cells, rather than by the existence of a drifting conductive lid. Since similar cell widening was reported in sluggish lid convection of bottom heating models (Kameyama and Ogawa, 2000; Okuda and Takehiro, 2023), the existence of sluggish lid convection driven by internal heating is thus conceivable. We will clarify the nature of the intermediate regime by a systematic exploration of convective solutions in the parameter space.

1.5 Motivation and thesis outline

	Constant viscosity	Temperature-dependent viscosity
Bottom heating	Studied since around 1900s Whole layer convection	e.g. Solomatov (1995) Mobile, Sluggish lid, Stagnant lid
Internal heating	e.g. Roberts (1967) Whole layer convection	This study Mobile, ?, Stagnant lid

Table 1.1: A summary of studies on thermal convection modeled for mantle convection.

We have reviewed the current status of the studies on fundamental mantle convection models, which is summarized in Table 1.1. The dynamical regimes and characteristics of solutions to the problem of internally heated convection with temperature-dependent viscosity have not been fully explored, especially for the sluggish lid structure in the intermediate parameter range. Therefore, in this study, we aim to understand different convective patterns of an internal heating system in each regime including the possible intermediate regime. Extensive parameter studies will help us understand how different structures of convection arise. Regime classification and characterization are of particular interest for this purpose. It is also interesting that different scaling relations are expected among the regimes, as well as in the bottom-heated system.

We use the Newton method to calculate steady-state solutions of finite-amplitude convection with internal heating (Okuda et al., 2025). This method is distinctively different from the time-integrating simulations employed in the previous studies. While it is sometimes difficult to judge whether time-dependent solutions obtained by time integration have reached steady state or not, solutions obtained by the

Newton method are analyzed more easily to be classified and characterized in terms of convective structures systematically. Moreover, we can obtain both stable and unstable steady solutions, providing insights into the framework of dynamical systems. For example, we can observe the transition from unstable fixed points to stable attractors. Actually, Okuda and Takehiro (2023) adopted this method for the bottom-heated convection problem and succeeded in developing the regime diagram of Solomatov (1995) to include the dependence of the horizontal wavelength in scaling relations.

This study mainly investigates the rheological model of the Frank-Kamenetskii (FK) approximation (1.2) to describe the effect of temperature dependence for the system with a single parameter about the variable viscosity. Then we examine the problems with the Arrhenius-law viscosity (1.1), and compare the results between these models.

Chapter 2 describes the mathematical model and the numerical method used in this study. Chapter 3 presents the steady-state solutions and their regime classification. Scaling relations are examined for each regime, and especially, solutions of the sluggish lid regime are characterized in detail. Chapter 4 discusses the following topics: the scaling relations for steady solutions explained by modifying the classical boundary layer theory; the stability of steady solutions; the effect of the top surface boundary conditions on the convective regimes; and a comparison of the regime diagrams with different viscosity systems. Chapter 5 presents the conclusion of this thesis.

Chapter 2

Governing equations and numerical method

2.1 Governing equations

We consider thermal convection of an incompressible fluid in a two-dimensional horizontal layer. The Prandtl number is taken as infinitely large and the Boussinesq approximation is adopted, as general assumptions of the planetary mantle. The domain is horizontally periodic with a length λ, and bounded by an adiabatic (i.e. zero heat flux) boundary at the bottom and an isothermal boundary at the top. Dimensionless variables are defined using the layer thickness d, thermal diffusion time d^2/κ, the viscosity at the top surface η_0, and the temperature scale Hd^2/k, with κ the thermal diffusivity, k the thermal conductivity and H the uniform volumetric heating rate. Because of the two-dimensional incompressible system, we can take a stream function ψ satisfying horizontal and vertical velocity u and v as

$$(u, v) = \left(-\frac{\partial \psi}{\partial y}, \frac{\partial \psi}{\partial x} \right). \tag{2.1}$$

The dimensionless equations governing stream function $\psi(x, y, t)$ and temperature $T(x, y, t)$ are (e.g. Christensen, 1984):

$$\frac{\partial T}{\partial t} = \frac{\partial (T, \psi)}{\partial (x, y)} + \nabla^2 T + 1, \tag{2.2}$$

$$\left(\frac{\partial^2}{\partial x^2} - \frac{\partial^2}{\partial y^2} \right) \left[\eta(T) \left(\frac{\partial^2}{\partial x^2} - \frac{\partial^2}{\partial y^2} \right) \psi \right] + 4 \frac{\partial^2}{\partial x \partial y} \left(\eta(T) \frac{\partial^2 \psi}{\partial x \partial y} \right) = -Ra_0 \frac{\partial T}{\partial x}, \tag{2.3}$$

$$\eta(T) = \exp\left(-\gamma T \right), \tag{2.4}$$

$$T = \psi = \frac{\partial^2 \psi}{\partial y^2} = 0 \quad \text{at } y = 1, \tag{2.5}$$

$$\frac{\partial T}{\partial y} = \psi = \frac{\partial^2 \psi}{\partial y^2} = 0 \quad \text{at } y = 0, \tag{2.6}$$

$$T(0, y, t) = T(\lambda, y, t), \quad \psi(0, y, t) = \psi(\lambda, y, t), \tag{2.7}$$

where $\nabla^2 = \frac{\partial^2}{\partial x^2} + \frac{\partial^2}{\partial y^2}$ is the two-dimensional Laplacian, and $\frac{\partial(T,\psi)}{\partial(x,y)} = \frac{\partial T}{\partial x}\frac{\partial \psi}{\partial y} - \frac{\partial T}{\partial y}\frac{\partial \psi}{\partial x}$ is the Jacobian of T and ψ. The Rayleigh(–Roberts) number is defined as (Roberts, 1967)

$$Ra_0 = \frac{\alpha \rho g H d^5}{\kappa k \eta_0}, \tag{2.8}$$

where α is the thermal expansion coefficient, ρ is the density, g is the gravitational acceleration, and k is the thermal conductivity.

The definition of the Rayleigh number Ra_0 is consistent with the classical expression for bottom-heated convection (e.g. Chandrasekhar, 1961)

$$Ra = \frac{\alpha \rho g \Delta T d^3}{\kappa \eta}, \tag{2.9}$$

using temperature scale Hd^2/k instead of ΔT. ΔT is temperature difference defined by bottom and top isothermal boundaries. In our problem, since temperature at the bottom surface is not fixed, temperature scale is given by internal heating rate.

2.2 Definitions of output parameters

We have defined two dimensionless input parameters Ra_0 and γ in the governing equations. We will calculate and examine solutions controlling the parameter set (Ra_0, γ). On the other hand, some variables will be useful that are defined using output quantities of T and ψ.

Viscosity contrast is a key parameter to characterize dynamical regimes as described in previous studies (see Section 1.3). Compared to the situation when the total temperature difference is imposed across the layer, the parameter γ is insufficient to quantify the viscosity contrast across the layer. We rather use the output value of T at the bottom surface to define viscosity contrast ratio r_η:

$$r_\eta = \frac{\eta_0}{\eta_b} = \exp(\gamma T_b), \tag{2.10}$$

where $\eta_b = \eta_0 \exp(-\gamma T_b)$ is (dimensional) viscosity at the bottom boundary and T_b

is temperature averaged on the bottom boundary. T_b is close to the temperature of the isothermal well-mixed convection core since there is no thermal boundary layer along the adiabatic bottom surface.

At large viscosity contrast, convection is in the stagnant lid regime where most of the temperature and viscosity contrasts are concentrated in the conductive lid. Since the Rayleigh number Ra_0 (2.8) is constructed using the viscosity at the upper boundary, it does not properly characterize the dynamics of the layer where convection actually occurs. We therefore introduce the bottom Rayleigh number, Ra_b, defined using η_b:

$$Ra_b = \frac{\alpha \rho g H d^5}{\kappa k \eta_b} = Ra_0 \frac{\eta_0}{\eta_b} = Ra_0 r_\eta. \tag{2.11}$$

The Nusselt number is the dimensionless heat flux on the top surface per unit horizontal length. As seen in eq. (1.3), scaling relations of it to parameters are useful to describe finite-amplitude convection. We define the Nusselt number using dimensionless output variables as

$$Nu = \frac{1}{T_b}, \tag{2.12}$$

which is the same definition as Solomatov and Moresi (2000). This is simply the reciprocal of the internal temperature of the convective region. Scaling relations of Nu are therefore essentially equivalent to that of the interior temperature in previous studies (e.g. Grasset and Parmentier, 1998; Hüttig and Breuer, 2011). Note that $Nu = 2$ corresponds to the hydrostatic state, because the conductive temperature profile, solving eqs. (2.2, 2.6, 2.5) with $\psi = 0$, is $T = (1 - y^2)/2$.

2.3 Numerical calculation of steady-state solutions

2.3.1 Numerical formulation

Second-order finite differences are used for the numerical formulation of the equations (2.2)–(2.7). In particular, the finite difference equation proposed by Andrews (1972) is used for the momentum equation (2.3), which is successful for discretizing the fourth order derivative of in the two-dimensional diffusion equation with a non-uniform diffusion coefficient.

The domain is discretized into square grids of lengths 1/32 or 1/64 for all numerical calculations. Most calculations in this study use the resolution of 1/32. For some cases for which iterative calculations do not converge, the resolution of 1/64 is used.

2.3.2 Numerical method for solving steady-state solutions

We obtain numerical steady-state solutions using the Newton method in the same procedure as that of Okuda and Takehiro (2023). Let the right hand side of the energy equation (2.2) be $F(T)$, so that a steady solution satisfies $F(T) = 0$. When $T(x, y)$ is given, $\psi(x, y)$ is obtained by solving the linear equation (2.3). $F(T)$ is thus a function of $T(x, y)$. The nonlinear equation $F(T) = 0$ is solved iteratively. At each iteration, a new estimate T_{new} of the steady solution is computed by solving the first-order Taylor expansion of $F(T)$ around the previous value T_{old} at each position $\vec{r} = (x, y)$ in the domain:

$$0 = F(T_{\text{old}})(\vec{r}) + \frac{\mathrm{d}F}{\mathrm{d}T}(\vec{r}, \vec{\xi}) \cdot \left(T_{\text{new}}(\vec{\xi}) - T_{\text{old}}(\vec{\xi})\right). \tag{2.13}$$

The derivative of $F(T)$ by T is calculated by finite numerical differentiation as

$$\frac{\mathrm{d}F}{\mathrm{d}T}(\vec{r}, \vec{\xi}) = \frac{F(T + \delta T_{\xi})(\vec{r}) - F(T)(\vec{r})}{\Delta}, \quad \delta T_{\xi}(\vec{r}) = \begin{cases} \Delta & (\vec{r} = \vec{\xi}), \\ 0 & (\vec{r} \neq \vec{\xi}). \end{cases} \tag{2.14}$$

Here, $\vec{\xi}$ is a position at which a small perturbation Δ is added to T. The value of Δ is given as 10^{-6} in this study. We set the convergence criterion for the calculation of the Newton method to ensure that the update of temperature for one iteration step $\max|T_{\text{new}} - T_{\text{old}}|$ becomes less than 1×10^{-6}, which is small enough compared to the typical amplitude of T variations of the order of $\sim 10^{-1}$.

Steady-state calculations are computed for the ranges of the parameters of $1 \leq Ra_0 \leq 10^6$ and $0 \leq \gamma \leq 40$. Solutions for $20 \leq \gamma \leq 30$ are explored in detail in order to focus on the solutions around the intermediate (sluggish lid) regime. Only solutions with horizontal wavelength $\lambda = 2$ are considered.

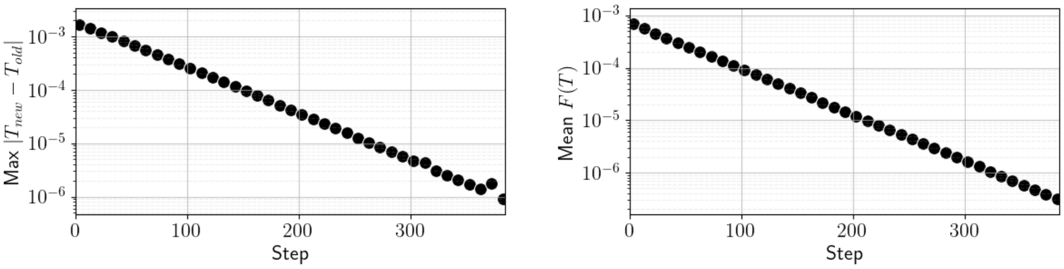

Figure 2.1: Example of convergence of the Newton method calculation. The maximum norm of temperature update $T_{new} - T_{old}$ by one step of iteration (left) and the averaged values of $F(T)$ (the right-hand side of eq. 2.2) over the whole layer (right) are shown for every ten steps of iteration.

2.3.3 Convergence of steady-state calculations

The convergence of an iterative calculation for a steady solution is shown in Figure 2.1. The calculation runs until the maximum norm of $\max|T_{\mathrm{new}} - T_{\mathrm{old}}|$ (shown in left panel) drops below the chosen convergence criterion, 1×10^{-6}. The right panel shows the averaged values of $F(T)$ in the whole domain. As the calculation converges, $F(T)$ decreases by several orders of magnitude. All steady solutions that will be shown in Chapter 3 successfully converge in this manner.

Chapter 3

Convective structures of steady solutions

3.1 Steady-state solutions and regime classification

We calculate steady-state finite-amplitude convective solutions by the method described in Section 2.3. Setting the resolution of 1/32, 610 cases of parameter sets successfully converge to finite amplitude solutions with the wavelength of $\lambda = 2$, and 27 cases at the resolution of 1/64. The left panel of Figure 3.1 shows the steady solutions on the controlled parameter space (Ra_0, γ) with colored plots (colors are described later). Black solid circles represent the neutral values of the linear stability analysis for the hydrostatic state, derived in Section A.1. The right panel of Figure 3.1 shows the diagram of Ra_b and r_η, both of which are output parameters defined in Section 2.2.

The obtained steady solutions are classified into three regimes, mobile, sluggish lid, and stagnant lid regimes with the top surface mobility M (Tackley, 2000), which is defined as the ratio of the root mean square of horizontal velocity at the top surface $u_{\mathrm{surface,rms}}$ to that in the whole layer u_{rms}, where

$$u_{\mathrm{rms}} = \sqrt{\int_0^\lambda \int_0^1 u^2 \mathrm{d}x \mathrm{d}y/\lambda}, \quad u_{\mathrm{surface,rms}} = \sqrt{\int_0^\lambda u(y=1)^2 \mathrm{d}x/\lambda}.$$

Then we define mobile, sluggish lid, and stagnant lid regimes as $M > 0.90$, $0.90 \geq M > 0.02$, and $0.02 \geq M$, respectively. The threshold values are somewhat arbitrary. The different regimes are expected to follow different scaling relations between the Nusselt number and the parameters such as the Rayleigh number and the temperature-dependence strength of viscosity. Scaling laws for the stagnant lid

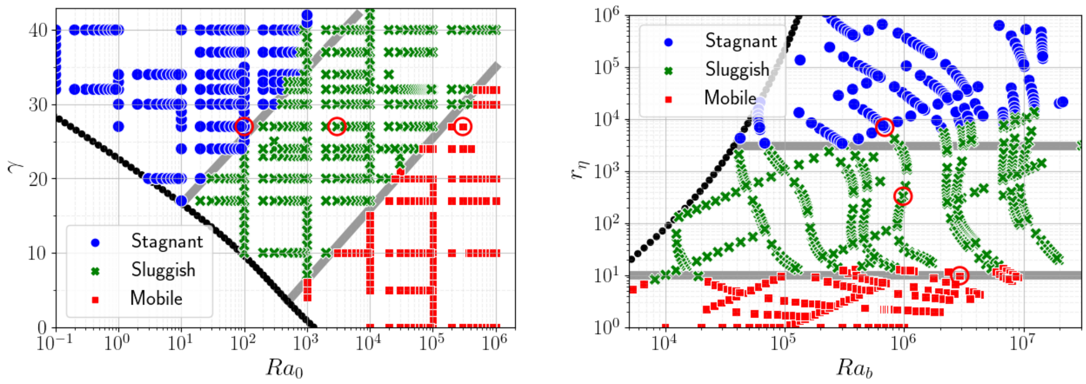

Figure 3.1: Steady solutions on the Ra_0–γ diagram (left) and the Ra_b–r_η diagram (right). Red, green, and blue symbols correspond to steady solutions classified into mobile, sluggish lid, and stagnant lid regimes, respectively. Black circles represent the neutral stability values for the hydrostatic conduction state (see A.1). Three red circles on each panel identify the cases whose convective structures are shown in Figures 3.2 and 3.3. The grey lines indicate the rough regime boundaries.

and mobile regimes are presented in Figure 3.6 in Section 3.3, and we adjust the threshold values of M such that they also match the validity limits of the scaling laws.

In both regime diagrams in Figure 3.1, three regimes appear to be clearly separated, in which regimes of each solutions are indicated by color. In the Ra_0–γ diagram (left), regimes are in banded forms in the direction from small Ra_0 and γ to large Ra_0 and γ. The mobile regime occupies a region with low γ or high Ra_0, the stagnant lid regime for high γ or low Ra_0, and the sluggish lid regime is in between. The regime boundaries in the Ra_b–r_η diagram (right) appear nearly constant values of r_η, $r_\eta \approx 1 \times 10^1$ for the mobile–sluggish lid boundary, and $r_\eta \approx 3 \times 10^3$ for the sluggish lid–stagnant lid boundary. The latter slightly changes from $r_\eta \approx 3 \times 10^3$ to 1×10^4 for Ra_b ranging from 4×10^4 to 1×10^7. The value of r_η for the sluggish lid–stagnant lid boundary is similar to that obtained by Hüttig and Breuer (2011) of $r_\eta \approx 10^4$ for internal heating convection in a spherical shell with a radius ratio of 0.55. As shown by Javaheri et al. (2024), viscosity contrast can strongly depend on the length ratio of spherical shell, at least for the bottom heating situation they considered.

The distribution of the three regimes for internal heating convection shown in the right panel of Figure 3.1 qualitatively agrees with previous results for the bottom heating, although the values of the regime boundaries are slightly different. Solomatov (1995) and Kameyama and Ogawa (2000) studied bottom heating convection of a two-dimensional temperature-dependent viscous fluid. They showed that the sluggish lid–stagnant lid boundary is at $r_\eta = 10^4$. The mobile–sluggish lid boundary in Solomatov (1995) increases slightly with the Rayleigh number, from $r_\eta \approx 10^0$ at $Ra_b = 10^3$ to $r_\eta \approx 10^3$ at $Ra_b = 10^{11}$, and that in Kameyama and Ogawa (2000) is independent of Ra_b but the value $r_\eta \approx 10^{3.5}$ is different from the one we get, $r_\eta \approx 10^1$. Okuda and Takehiro (2023) showed the regime boundaries of steady-state bottom heating convection with a horizontal wavelength of 2 as $r_\eta = e^{1.5} \approx 5$ for the mobile–sluggish lid boundary and $r_\eta = e^{8.0} \approx 3 \times 10^3$ for the sluggish lid–stagnant lid boundary.

3.2 Structures of convection in each regime

Temperature Stream function

Mobile regime ($Ra_0 = 3 \times 10^5, \gamma = 27$)

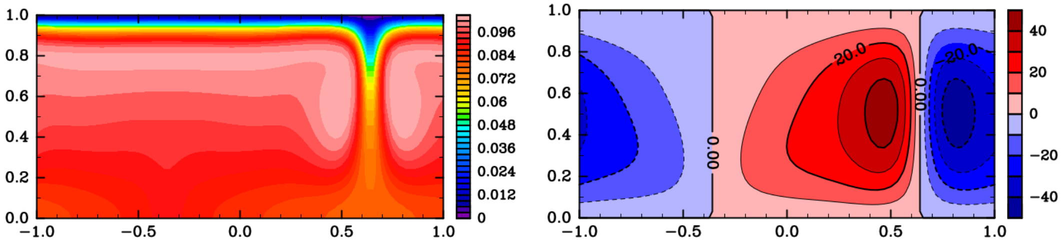

Sluggish lid regime ($Ra_0 = 3 \times 10^3, \gamma = 27$)

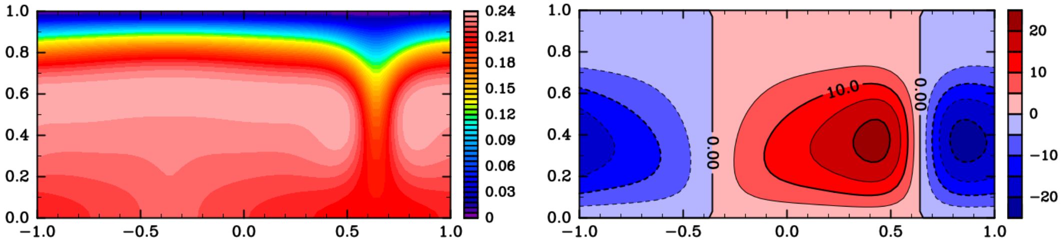

Stagnant lid regime ($Ra_0 = 1 \times 10^2, \gamma = 27$)

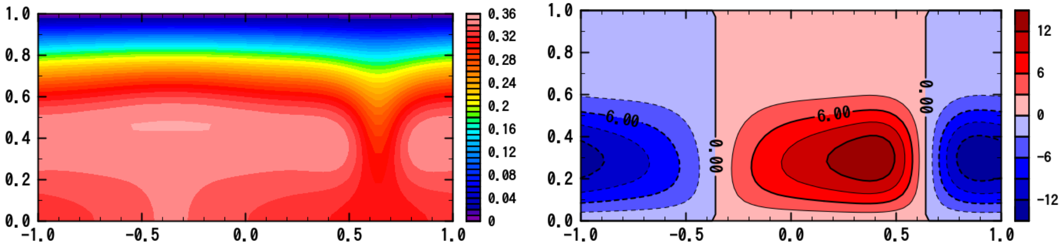

Figure 3.2: Examples of steady solutions of mobile (top), sluggish lid (center), and stagnant lid regimes (bottom). Temperature and stream function are shown in the left and right panels, respectively. Parameters Ra_0 and γ are indicated above each pair of panels.

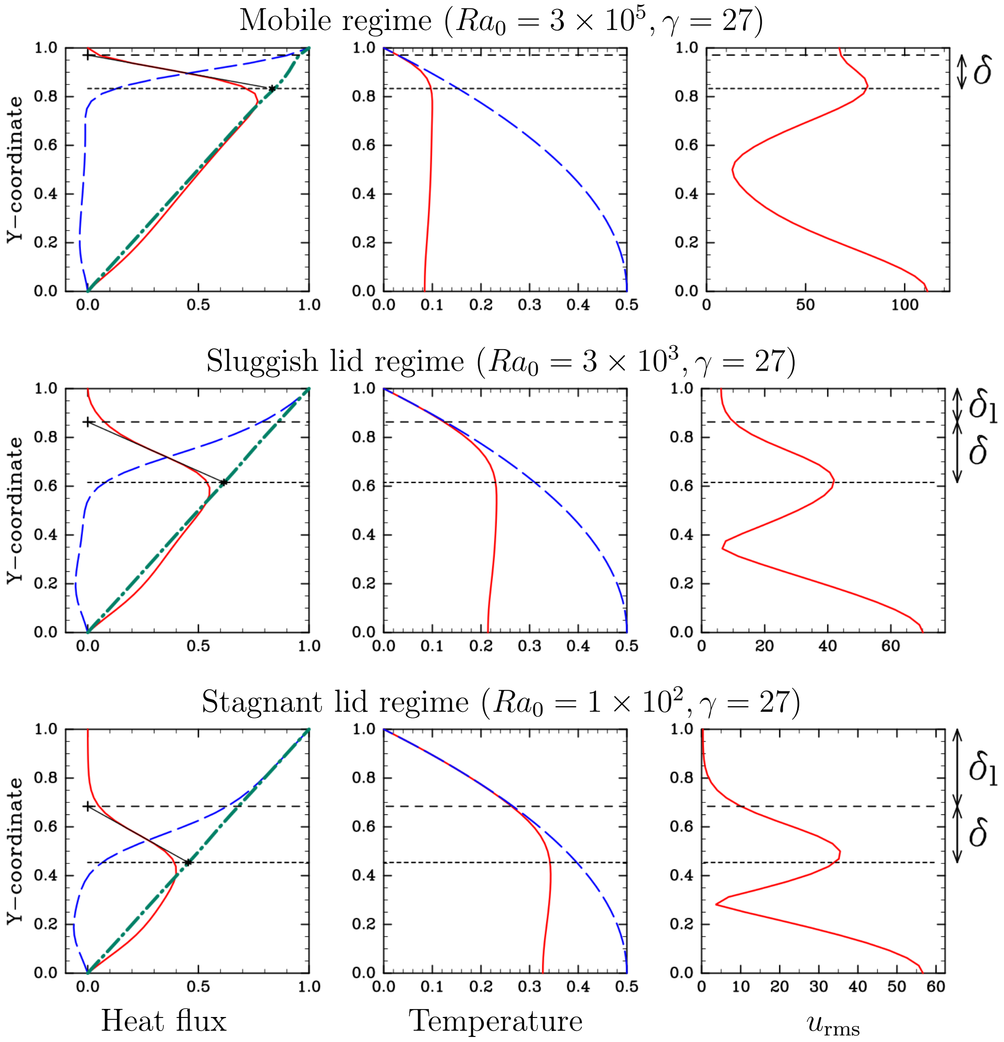

Mobile regime ($Ra_0 = 3 \times 10^5, \gamma = 27$)

Sluggish lid regime ($Ra_0 = 3 \times 10^3, \gamma = 27$)

Stagnant lid regime ($Ra_0 = 1 \times 10^2, \gamma = 27$)

Figure 3.3: Vertical profiles of several variables of steady solutions in mobile (top), sluggish lid (middle), and stagnant lid regimes (bottom). The left panels show horizontally averaged advection heat flux $\overline{vT}$ (red solid lines), diffusion heat flux $\overline{\partial_y T}$ (blue broken lines), and total heat flux (green dash-dotted lines). The middle column displays the horizontally averaged temperature $\overline{T}$ (red solid line) and the static conductive temperature (blue dashed line). The right panels show the root mean square $u_{\rm rms}$ of the horizontal velocity u for each height. The horizontal dashed and dotted lines in each panel show the boundaries between the conductive lid, active boundary layer and convective core. They are obtained as a crossing between straight-line fits to the advection profile in each region (see text for details). The thicknesses δ_l and δ of the lid and active boundary layer, respectively, are defined on the right-hand-side of the figure.

Typical solutions of finite-amplitude convection in each regime at the points indicated by red circles in Figure 3.1 are shown in Figures 3.2 and 3.3. Figure 3.2 shows temperature (left) and stream function (right) fields of mobile regime (top), sluggish lid regime (middle), and stagnant lid regime (bottom). Only a cold plume with strong downward flow develops because the thermal boundary layer exists along the isothermal surface. The thickness of the thermally conductive layer above the convective region increases from the mobile regime solutions to the stagnant lid regime solutions.

The vertical profiles of the horizontally averaged advection flux $\overline{vT}$ (red solid lines) and diffusion flux $\overline{\partial_y T}$ (blue broken lines) are shown in the left panels of Figure 3.3. The over-line means horizontal average that is $\overline{f}(y) = (1/\lambda)\int_0^\lambda f(x,y)\mathrm{d}x$. The green dash-dotted lines are total heat flow across each horizontal plane. By virtue of the conservation of energy (eq. 2.2) in steady state, it is $\overline{vT}+\overline{\partial_y T} = y$, which is equal to the total heat production below height y. Two horizontal thin dashed lines for each left panel divide from top to bottom a conductive lid (of thickness δ_l), an active boundary layer (of thickness δ), and an isothermal core. To objectively determine the height of these boundaries, the advection heat flux is approximated as a piecewise affine profile. Let $\overline{vT}$ in the active boundary layer $\overline{vT} = ay+b$ be defined by the tangent line at the inflection point (thin black solid lines). The stagnant lid being defined as a region where $\overline{vT} = 0$, its bottom boundary is the contact point of the advection heat flux on the y axis ($ay+b = 0$, shown by + in the left panels). The bottom of the active boundary layer is defined as the intersection of the advection tangent with the total heat flux, so the height is where $ay + b = y$ is satisfied ($*$ in the left panels). The conductive lid, boundary layer, and isothermal core defined in this way can be considered as regions where $\overline{vT} = 0$, $\overline{vT}$ and $\overline{\partial_y T}$ are comparable, and $\overline{\partial_y T} = 0$, respectively.

The middle and right panels of Figure 3.3 show the horizontal mean temperature $\overline{T}$ (red solid lines in the middle columns), the conductive temperature T_0 (eq. A.1, blue dashed lines), and the root mean square u_{rms} of horizontal velocity at each height (red lines in the right columns). From the profiles of u_{rms}, we can find that the velocity gradient in the conductive lid is small regardless of whether the lid moves or not. The velocity gradient is large in the boundary layer and in the isothermal core, but the temperature gradient driving the convective flow is concentrated in the boundary layer.

3.3 Scaling functions of mobile regime and stagnant lid regime

Here, we examine whether the steady solutions obtained in the mobile regime and the stagnant lid regime are consistent with the scaling relations proposed by the previous studies. Grasset and Parmentier (1998) (hereafter GP98) analyzed the data obtained by their numerical time integrating simulations and obtained the following relations, with replacement of the notation, for the solutions in the no-lid regime (eq. 14 in GP98) and in the conductive lid regime (eq. 29 in GP98), respectively.

$$T_b = a_m r_\eta^{\alpha_m} Ra_b^{-\beta_m}, \tag{3.1}$$

$$\tilde{T}_b = a_s \widetilde{Ra}_b^{-\beta_s}. \tag{3.2}$$

Here α_m, β_m, and β_s denote the exponents that are determined later by fitting these functions to our numerically obtained steady solutions. The tilde expresses the rescaled variable for the stagnant lid regime using a length scale equal to the height of the convective region $1-\delta_l$, expecting the same scaling relation inside the convective region as for iso-viscous convection, where δ_l is the thickness of the conductive lid defined by the advection flux profile (see Figure 3.3). Specifically, the viscosity ratio across the convective region, $r_{\eta\mathrm{eff}}$, is assumed to be constant according to GP98. Applying the energy balance in the conductive lid, the hight of convective region is written as (eqs. 23 and 28 of GP98)

$$1-\delta_l = \sqrt{1-2(T_b - \ln(r_{\eta\mathrm{eff}})/\gamma)}, \tag{3.3}$$

and other rescaled variables are as follows.

$$\tilde{T}_b = \frac{\ln(r_{\eta\mathrm{eff}})}{\gamma(1-\delta_l)^2}, \quad \widetilde{Ra}_b = Ra_b(1-\delta_l)^5, \quad \tilde{\delta} = \frac{\delta}{1-\delta_l}, \quad \tilde{u} = u(1-\delta_l). \tag{3.4}$$

Using the scaling functions (3.1) and (3.2), T_b is related to the input parameter Ra_0 and γ with the following equations, respectively for the mobile and stagnant lid regimes:

$$T_b \exp(-\alpha_m \gamma T_b) = a_m Ra_0^{-\beta_m} \exp(-\beta_m \gamma T_b), \tag{3.5}$$

$$\frac{\ln(r_{\eta\mathrm{eff}})}{\gamma}\left[1-2\left(T_b - \frac{\ln(r_{\eta\mathrm{eff}})}{\gamma}\right)\right]^{\frac{5}{2}\beta_s - 1} = a_s Ra_0^{-\beta_s} \exp(-\beta_s \gamma T_b). \tag{3.6}$$

Alternatively, the right hand side of both equations can be written as $aRa_b^{-\beta}$, which means that the scaling laws can be written in terms of either Ra_0 or Ra_b.

In order to examine the consistency of our results with the scaling relations of GP98. We fitted the function (3.1) to mobile regime solutions to obtain the best fit values of α_m, β_m, and a_m. As a result, two different sets of coefficients are derived depending on the value of Ra_b: $\alpha_m = 0.167$, $\beta_m = 0.255$, and $a_m = 1.82$ for $Ra_b < 10^5$, and $\alpha_m = 0.159$, $\beta_m = 0.164$, and $a_m = 0.652$ for $Ra_b \geq 10^5$. Figure 3.4 shows solutions in the $T_b r_\eta^{-\alpha_m}$–Ra_b space for the mobile regime. The value of $T_b r_\eta^{-\alpha_m}$

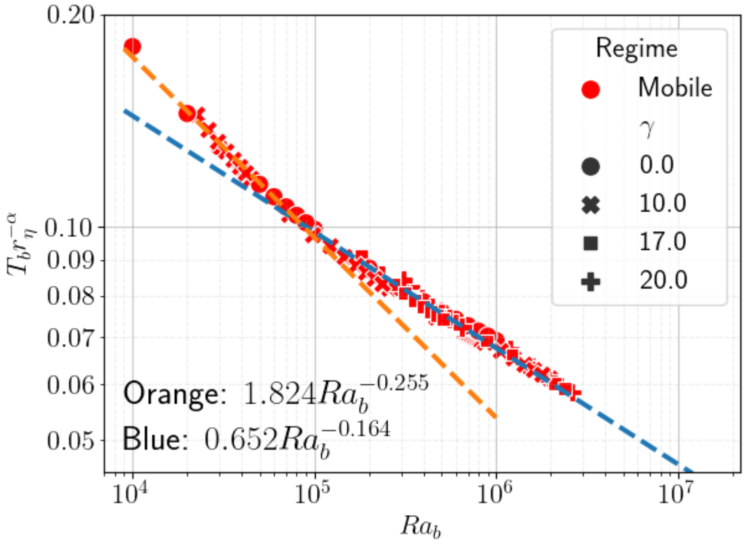

Figure 3.4: $T_b r^{-\alpha_m}$–$Ra_b^{-\beta}$ diagram for the solutions in the mobile regime. Two dash-dotted lines are the functions of eq. (3.1) fitted to solutions of $Ra_b < 10^5$ (orange) and $Ra_b > 10^5$ (blue). The best fit values of coefficients in eq. (3.1) are explained in Section 3.3. Value of $T_b r_\eta^{-\alpha_m}$ for each solution is calculated using $\alpha_m = 0.167$ for $Ra_b < 10^5$ and $\alpha_m = 0.159$ for $Ra_b \geq 10^5$.

for each solution is calculated using obtained value of α_m depending on Ra_b. Two dashed lines correspond to function (3.1) with different sets of coefficients. The results with different values of γ collapse on either of them.

Figure 3.5 shows the $\tilde{T}_b$-$\widetilde{Ra}_b$ plot for the solutions in the stagnant lid regime. $r_{\eta\mathrm{eff}}$ in eq. (3.4) is fixed to 5.4 based on the observation of our stagnant lid regime solutions, which will be described in Figure 3.8 in Section 3.4. We performed the power law fitting to obtain the best fit values of coefficients as $\beta_s = 0.167$ and $a_s = 0.929$. The value of β_s is very close to the exponent of mobile regime for $Ra_b \gtrsim 10^5$. The dashed line in Figure 3.5 shows the obtained power function. The power-law fitting explains well the solutions with $\widetilde{Ra}_b \lesssim 10^6$. On the other hand, there appears to be a misfit for the solutions with $\widetilde{Ra}_b \gtrsim 10^6$ ($\gamma = 40$), possibly due to the loose regime classification with mobility M (see Section 3.1). These solutions are close to the boundary with the sluggish lid regime and could be classified in that regime if a different threshold value of M was chosen.

We obtained a power function with the exponent of $\beta_m = 0.255$, which mobile regime solutions for $Ra_b \lesssim 10^5$ follow. This exponent is consistent with the classical scaling relation $Ra_b^{-1/4}$ for internally heated iso-viscous convection (e.g. Parmentier et al., 1994; Turcotte and Schubert, 2014) and no-lid regime convection of GP98. On the other hand, solutions of $Ra_b \gtrsim 10^5$ follow the power law functions with

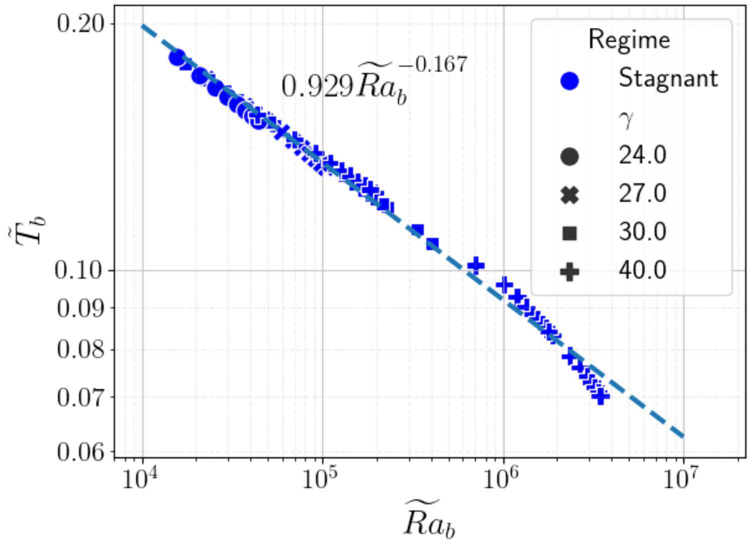

Figure 3.5: $\tilde{T}_b$-$\widetilde{Ra}_b$ diagram for the solutions in stagnant lid regime. The dash-dotted line is the result of the power-law fitting of the function (3.2) to data of stagnant lid regime solutions with different values of Ra_0 and some fixed values of γ. $r_{\eta\mathrm{eff}}$ in eq. (3.4) is set as a constant value 5.4 based on our observation of $r_{\eta\mathrm{eff}}$ (see Figure 3.8).

$\beta \approx 1/6$ for both the mobile and stagnant lid regimes. The difference between time-dependent and steady solutions may cause this smaller exponent. Section 4.1 discusses this issue in detail.

Using the coefficients obtained above, Figure 3.6 shows the scaling relation curves for $\gamma = 20$ of the mobile regime (eq. 3.5) and $\gamma = 30$ of the stagnant lid regime (eq. 3.6) in the Nu–Ra_b space together with steady solutions for several values of γ as examples. Nu and Ra_b are given by Eqs. (2.12) and (2.11). The functions of the mobile and stagnant lid regimes fit well to the solutions of respective regimes, including other setting of γ. Note that solutions in the sluggish lid regime do not follow any of the scaling functions obtained for the mobile and stagnant lid regimes, for any fixed value of γ, even though the curves for other values of γ are not displayed in Figure 3.6. The data of sluggish lid regime solutions show that Nu increases rapidly with a small change of Ra_b for each value of γ. To explore each γ branch, we vary monotonically the input control parameter Ra_0, but Ra_b, which depends on the value of T_b actually realized, does not necessarily increase monotonically. Solutions in the sluggish lid regime are characterized in detail in Section 3.4.

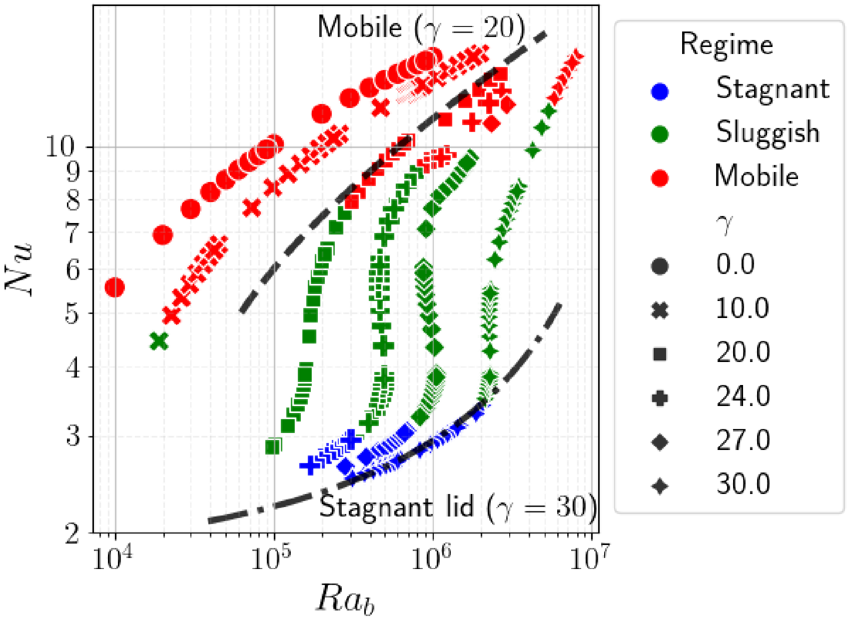

Figure 3.6: Steady solutions for several values of γ on Nu–Ra_b plane. Colors represent the regime of each solution. The Nusselt number Nu and the Rayleigh number Ra_b are defined by eqs. (2.12) and (2.11). The scaling relations of the stagnant lid regime (dash-dotted, eq. 3.6) and the mobile regime (dashed, eq. 3.5) are overlaid. The coefficient and exponents in these equations are determined in Section 3.3, and γ is fixed as indicated values near each curve. Note that Ra_b does not necessarily increase monotonically even if Ra_0 increases.

3.4 Characterization of sluggish lid regime

To specify different characteristics of the sluggish lid regime, two variables that are related to thermal structures of convection are shown in Figures 3.7 and 3.8. Figure 3.7 shows the height of the convective region, $1 - \delta_l$, as a function of Ra_b for several values of γ, where δ_l is the thickness of the conductive lid defined in Section 3.1 (see Figure 3.3). For any given value of γ, starting in the stagnant lid regime at low values of Ra_b, the height of the convective region increases steadily with increasing Ra_0 and therefore with Ra_b. This corresponds to an increase of intensity of convection. When entering the sluggish lid regime, increasing Ra_0 leads to a rapid increase of $1 - \delta_l$ (decrease of δ_l toward 0) at a nearly constant value of Ra_b. Upon further increase of the Rayleigh number, the system enters in the mobile regime where the height of the active convective region gets close to unity. However, $1 - \delta_l$ does not reach 1 and saturate at y_{sat}, contrary to the physical insight that the conducting lid should disappear in the mobile regime. This stems from our definition of the conductive lid by approximating $\overline{vT}$ with the piecewise linear profile, while

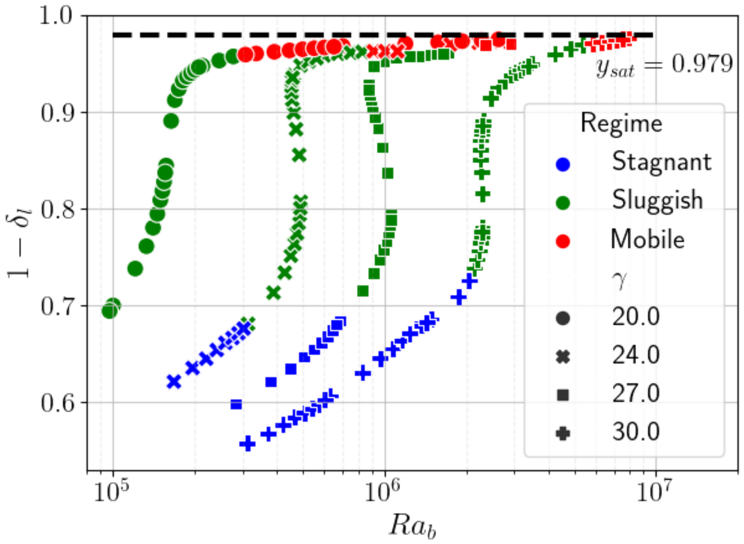

Figure 3.7: The height of the convective region $1-\delta_l$ as a function of Ra_b for the solutions of $\gamma = 20, 24, 27$, and 30. δ_l is the thickness of the conductive lid defined by advection heat flux profile (see Figure 3.3). The dashed line shows the maximum value of $1-\delta_l$.

$\overline{vT}$ actually behaves as a quadratic function of the distance from the top surface near $y = 1$.

Figure 3.8 shows the viscosity contrast across the convective region $r_{\eta\text{eff}}$, as a function of Ra_b for the same solutions as used in Figure 3.7. The value of $r_{\eta\text{eff}}$ for each data is calculated as a ratio of viscosity $\eta\left(\overline{T}(y = 1-\delta_l)\right)/\eta\left(\overline{T}(y = 0)\right)$. We observe that the viscosity contrast is almost constant, $r_{\eta\text{eff}} \approx 5.4$, for the solutions in the stagnant lid regime, which is consistent with the results of previous studies. Davaille and Jaupart (1993) found a constant viscosity contrast ratio across the convective region below the conductive lid. GP98 analyzed the solutions of stagnant lid regime and obtained the best-fitted value of $e^{2.23} \approx 9.3$, which is about twice our result. Mobile regime solutions have smaller values of $r_{\eta\text{eff}}$ than 5.4 because temperature difference T_b decreases (or the Nusselt number increases) when the Rayleigh number increases.

The most remarkable feature in Figure 3.8 is the high values of $r_{\eta\text{eff}}$ for the solutions in the sluggish lid regime compared to those for the solutions in the mobile and stagnant lid regimes. When the solutions change from the stagnant lid regime to the sluggish lid regime, the values of $r_{\eta\text{eff}}$ increase at first, and reach a maximum in the middle of the sluggish lid regime for each value of γ. Upon further increase of Ra_b, $r_{\eta\text{eff}}$ decreases and the system leaves the sluggish lid regime for the mobile regime, where $r_{\eta\text{eff}}$ reaches the one in the stagnant lid regime.

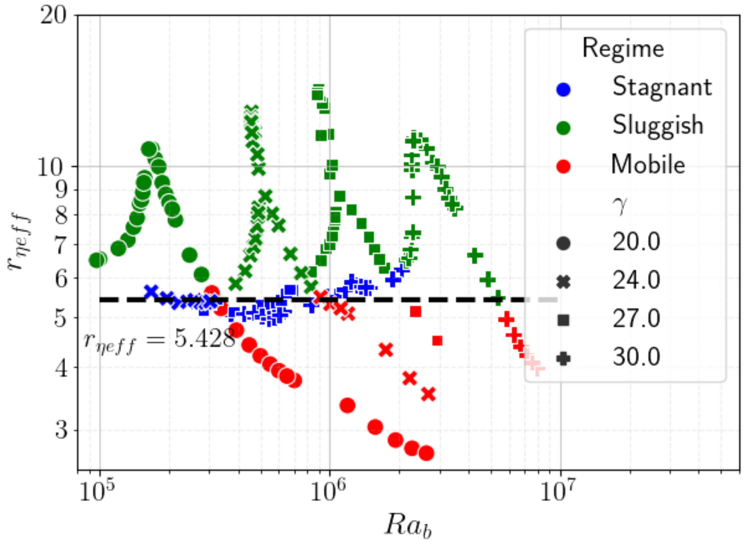

Figure 3.8: Viscosity contrast ratio across the convective region $r_{\eta\mathrm{eff}}$, as a function of Ra_b for the solutions of $\gamma = 20, 24, 27$, and 30. The dashed line expresses the average value of $r_{\eta\mathrm{eff}}$ for stagnant lid regime solutions.

From these results, convection in the sluggish lid regime can be characterized as a rapid increase of Nu with Ra_b compared to the scaling relations of the mobile and stagnant lid regimes, where the height of convection increases and Ra_b remains almost constant even if Ra_0 is changed. In the sluggish lid regime, a larger value of $r_{\eta\mathrm{eff}}$ is reached compared to the nearly constant value obtained in the stagnant lid regime. The assumption of constant $r_{\eta\mathrm{eff}}$ for the stagnant lid regime by GP98 is based on the existence of a motionless conductive lid, so that the feature of larger $r_{\eta\mathrm{eff}}$ for the sluggish lid regime may relate to the mobility of a conductive lid, which will be discussed in Section 4.3.

Chapter 4

Discussions

4.1 Scaling relations for steady convection with a strong downward plume

Table 4.1 summarizes the results of the fitted scaling functions obtained in Section 3.3 in the "δ, T_b" and "$\tilde{\delta}, \tilde{T_b}$" rows of the "Numerical results" column. The functions of bottom temperature T_b and rescaled one $\tilde{T_b}$ are referred to Figures 3.4 and 3.5, respectively. In Section 3.3, we found that the power of the Rayleigh number, β_m and β_s, in eqs. (3.1) and (3.2) for the high-Ra_b mobile regime and the stagnant lid regime are different from those proposed by GP98 ("GP98" column). The exponent $\beta_m = 0.255$ of our low-Ra_b mobile regime is almost the same as 0.227 of GP98, while β_m and β_s are about 1/6 for other cases of our calculations. The power law with $\beta = 1/4$ can be explained by the classical boundary layer theory (Turcotte and Schubert, 2014), while $\beta = 1/6$ has not been obtained in previous studies. We propose the following discussions for the cases of the lower exponent scaling law of internal heating convection.

Figure 4.1 compares the flow structures and viscous dissipation distribution for small and large values of the Rayleigh number, $Ra_b = 1 \times 10^4$ and $Ra_b = 1 \times 10^6$, in the mobile regime. Distribution of viscous dissipation is one of the key points for obtaining scaling relations (e.g. Solomatov, 1995). Viscous dissipation $\Phi(x, y)$ is defined as

$$\Phi(x,y) = \sum_{i,j=x,y} \eta \left(\frac{\partial u_i}{\partial x_j} + \frac{\partial u_j}{\partial x_i} \right) \frac{\partial u_i}{\partial x_j}. \tag{4.1}$$

Steady convection with high $Ra_b \gtrsim 10^5$ typically has a strong and thin downward plume (right panel of Figure 4.1), while convection with $Ra_b \lesssim 10^5$ has almost symmetric stream lines (left panel of Figure 4.1). Such a symmetric shape of the

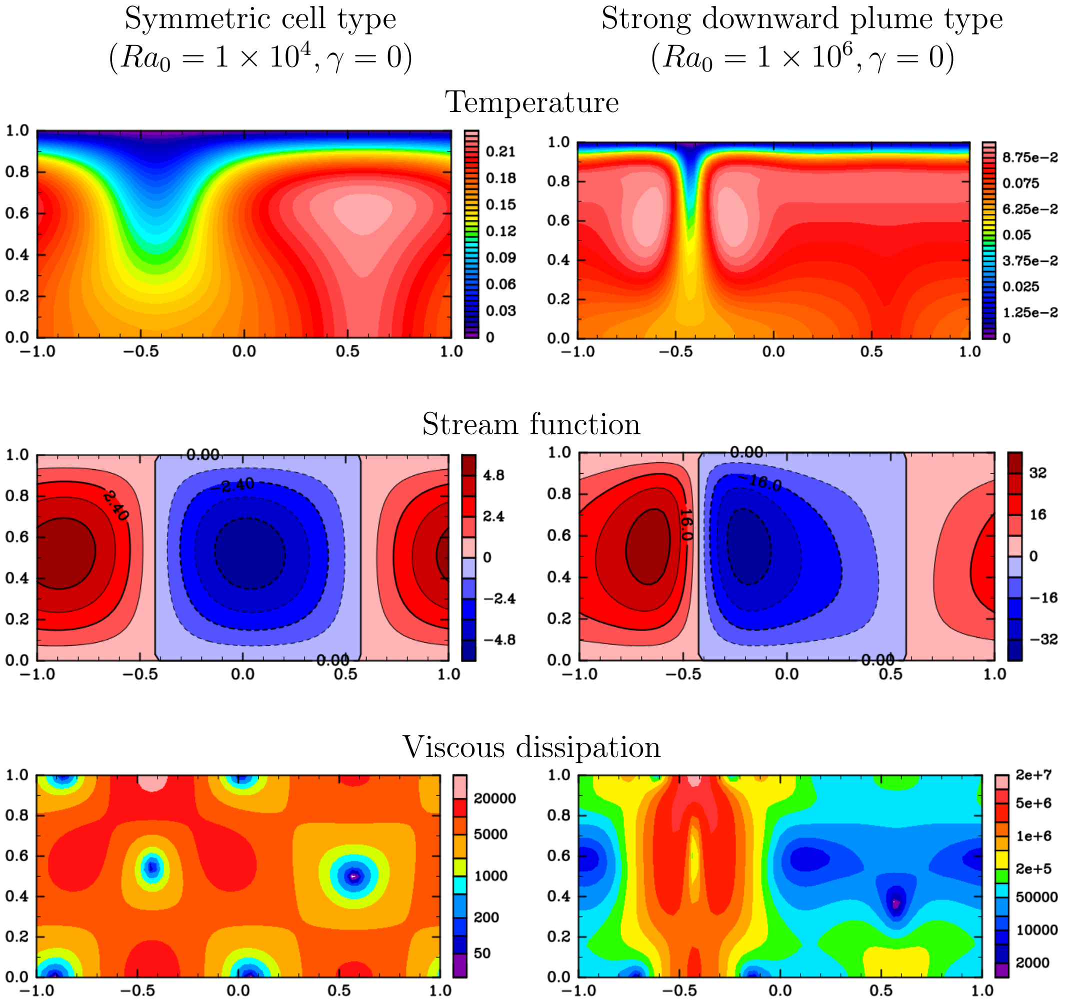

Symmetric cell type ($Ra_0 = 1 \times 10^4, \gamma = 0$)

Strong downward plume type ($Ra_0 = 1 \times 10^6, \gamma = 0$)

Temperature

Stream function

Viscous dissipation

Figure 4.1: Examples of solutions with two types of convection; symmetric cell convection (left panels, the solution of $\gamma = 0$ and $Ra_b = 1.0 \times 10^4$), and convection which has strong downward plume (right panels, $\gamma = 0$ and $Ra_b = 1.0 \times 10^6$). The temperature, stream function, and viscous dissipation are shown from top to bottom.

	Numerical results	Theory	GP98
Mobile regime ($Ra_b < 10^5$)			
δ, T_b	$r_\eta^{0.167} Ra_b^{-0.255}$		$r_\eta^{0.155} Ra_b^{-0.227}$
Mobile regime ($Ra_b > 10^5$)			
δ, T_b	$r_\eta^{0.159} Ra_b^{-0.164}$	$r_\eta^{1/6} Ra_b^{-1/6}$	$r_\eta^{0.155} Ra_b^{-0.227}$
u	$r_\eta^{-0.30} Ra_b^{0.339}$	$r_\eta^{-1/3} Ra_b^{1/3}$	
$\int \Phi \mathrm{d}V \sim \left(u/\delta\right)^2$	$r_\eta^{-0.92} Ra_b^{1.01}$	$r_\eta^{-1} Ra_b^{1}$	
Stagnant lid regime			
$\tilde{\delta}, \tilde{T}_b$	$\widetilde{Ra}_b^{-0.167}$	$\widetilde{Ra}_b^{-1/6}$	$Ra_b^{-0.227}$
$\tilde{u}$	$\widetilde{Ra}_b^{0.371}$	$\widetilde{Ra}_b^{1/3}$	
$\int \widetilde{\Phi} \mathrm{d}\widetilde{V} \sim \left(\tilde{u}/\tilde{\delta}\right)^2$	$\widetilde{Ra}_b^{1.07}$	$\widetilde{Ra}_b^{1}$	

Table 4.1: Summary of scaling functions for the mobile and stagnant lid regimes. δ is the active boundary layer thickness (see Figure 3.3). u is RMS of the horizontal velocity taken at the height where the maximum of u locates. Total viscous dissipation $\int \Phi \mathrm{d}V$ scales $\sim (u/\delta)^2$. Variables with a tilde are rescaled for the stagnant lid regime defined by eq. (3.4) using a length of the height of the convective region $1 - \delta_l$. The functions of the "Numerical results" column are derived from Figures 3.4, 3.5, and 4.2, while those of the "Theory" column are derived in Section 4.1.

convection cell has been assumed in the theory leading to the 1/4 power law for iso-viscous internal heating convection (Turcotte and Schubert, 2014). The difference in the viscous dissipation distributions is clearly seen in the bottom panels of Figure 4.1. Similar asymmetric flow has been observed by McKenzie et al. (1974) with an internal heating configuration, and they found a lower exponent than 1/4 as well. Solomatov and Moresi (2000) investigated stagnant lid convection by time integration, however, they did not find a solution with asymmetry, and suggested that such solutions are unlikely to be stable. The stability of steady solutions in time-dependent calculations will be discussed in Section 4.2. Based on these flow and viscous dissipation distributions, we will follow and revise the derivation of scaling relations of the classical boundary layer theory. In order to include the effect of the thinner plumes, the typical length scale of the horizontal velocity gradient is considered to be the boundary layer thickness rather than the entire wavelength of the convection cells.

First, in the mobile regime, in the upper thermal boundary layer, the balance between horizontal thermal advection, $u \cdot \nabla T \sim uT/\lambda$, and vertical diffusion, $\nabla^2 T \sim T/\delta^2$ is assumed. This gives $u \sim \delta^{-2}$, where u and δ are the typical amplitude of the horizontal velocity and the thickness of the boundary layer below the top surface or conductive lid. Taking into account the thin downward plume, we assume that the lateral variations of velocity concentrate on a width proportional to δ rather than

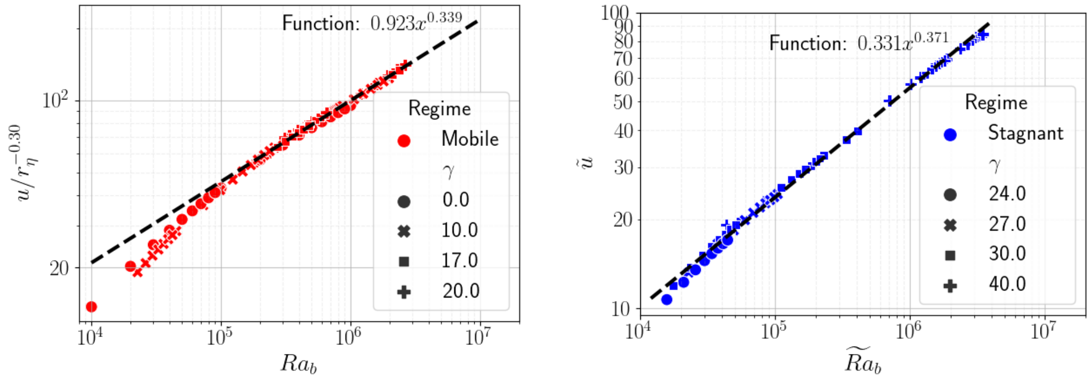

Figure 4.2: (Left) $u/r_\eta^{-0.3}$ versus Ra_b diagram for the solutions in the mobile regime, where u is the root mean square of the horizontal velocity taken at the height where the maximum of u is located. The dashed line shows a power law function fitted to the solutions for $Ra_b > 10^5$. (Right) $\tilde{u}$ versus $\widetilde{Ra}_b$ diagram for the solutions in the stagnant lid regime. The tilde indicates rescaled variables (eq. 3.4) in the active convective region. The dashed line shows a power law function fitted to all plotted solutions.

on a width proportional to the wavelength of the convective cells. The amplitude of the velocity gradient is evaluated as u/δ, and the total viscous dissipation $\int \Phi \mathrm{d}V \sim \eta(u/\delta)^2 \sim \delta^{-6}$. Finally, the energy balance relation $\int \Phi \mathrm{d}V = Ra_0 \int vT\mathrm{d}V = r_\eta^{-1} Ra_b$ holds exactly, and $\delta \sim r_\eta^{1/6} Ra_b^{-1/6}$ is obtained. T_b follows the same scaling as δ (δ, T_b of the "Theory" column for "Mobile regime ($Ra_b > 10^5$)" in Table 4.1). We can follow the same procedure for the stagnant lid regime using the variables rescaled by the height of the convective region (eq. 3.4). It can be seen that the lower exponent of the power of the Rayleigh number for T_b and δ, $-1/6$, is successfully derived ($\tilde{\delta}, \tilde{T}_b$ of the "Theory" column for the stagnant lid regime in Table 4.1). The theoretical scaling relations for other variables are also described in the "Theory" column as well.

To confirm the scaling relations of the horizontal velocity, Figure 4.2 shows the relations of the horizontal velocity u to the Rayleigh number Ra_b and $\tilde{u}$ to $\widetilde{Ra}_b$. u and $\tilde{u}$ are calculated as the root mean square of the horizontal velocity at the height where it is largest. For the mobile regime (left panel of Figure 4.2), the solutions for $Ra_b > 10^5$ are fitted to a power law function of r_η and Ra_b, and they successfully collapse on a single function $u \sim r_\eta^{0.30} Ra_b^{0.339}$ with different values of γ. Note that the scaling laws developed in this section is for large values of the Rayleigh number, since they require the flow to be characterized by a thin plume. This explains the discrepancy observed between the scaling laws and the numerical results at low values of $Ra_b < 10^5$. For the stagnant lid regime (right panel of Figure 4.2), all solutions lie on a fitted line $\tilde{u} \sim \widetilde{Ra_b}^{0.371}$.

The scaling relations of the horizontal velocity and total viscous dissipation estimated from our numerical steady solutions are additionally summarized in the column “Numerical results” of Table 4.1. The scale of the total viscous dissipation is obtained as $(u/\delta)^2$. Comparing the columns “Numerical results” and “Theory” of Table 4.1, the theoretical scaling relations of these variables are consistent with those obtained from the numerical steady solutions, although there is a slightly larger discrepancy in the exponent of $\tilde{u}$ of the stagnant lid regime compared to other variables.

4.2 Stability of steady solutions

High Ra_b convection observed in laboratory experiments (Davaille and Jaupart, 1993) and time-dependent simulations (e.g. GP98; Solomatov and Moresi, 2000) is intermittent with chaotic plumes. It seems that the width of convection cells for time-dependent convection is narrower than that of high Ra_b steady solutions presented here (e.g. Figures 3.2 or 4.1). Moreover, we have seen the high values of $r_{\eta\mathrm{eff}}$ in the sluggish lid regime presented by Figure 3.8 in Section 3.4. This implies that sluggish lid regime solutions have large temperature difference and thick boundary layers compared to the other regimes, and might become unstable due to the Rayleigh–Taylor instability. In this section, we examine the stability of steady solutions to evaluate convective structures that appear in time-evolving situations.

We perform time integration calculations starting some steady solutions. The time-dependent equations are eqs. (2.2) to (2.7). Each calculation is started from the given steady solution adding a small pointwise disturbance with the amplitude of $T \times 10^{-3}$ for T at the center of the domain. Time integrations are performed until $t = 10$ with a time step of $\Delta t = 10^{-6}$. Steady solutions are qualified as stable if they evolve back to their initial steady state, and unstable if they become time-dependent or reach a steady state that differs from the starting one.

The results in terms of stability are presented in Figure 4.3. Stable and unstable steady solutions are found in all regimes. The stability threshold looks to be located at $Ra_b \approx 10^6$; steady solutions with $Ra_b \lesssim 10^6$ remain stable, and those with $Ra_b \gtrsim 10^6$ become unstable regardless of the regimes. For all the cases of unstable solutions, periodic growth of cold plumes from the active boundary layer is observed.

A typical time evolution of the temperature field of an unstable solution ($Ra_0 = 10^4$ and $\gamma = 40$) is shown in Figure 4.4. It can be observed that a small downward

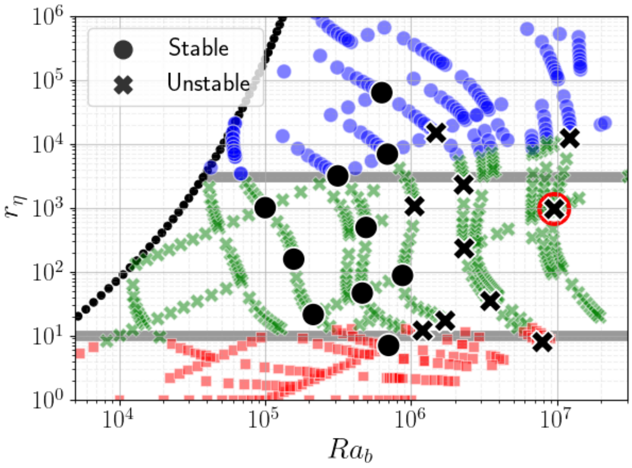

Figure 4.3: Stability of steady solutions. Black circles and crosses express stable and unstable solutions, respectively. A red circle identifies the solution which is shown in Figure 4.4.

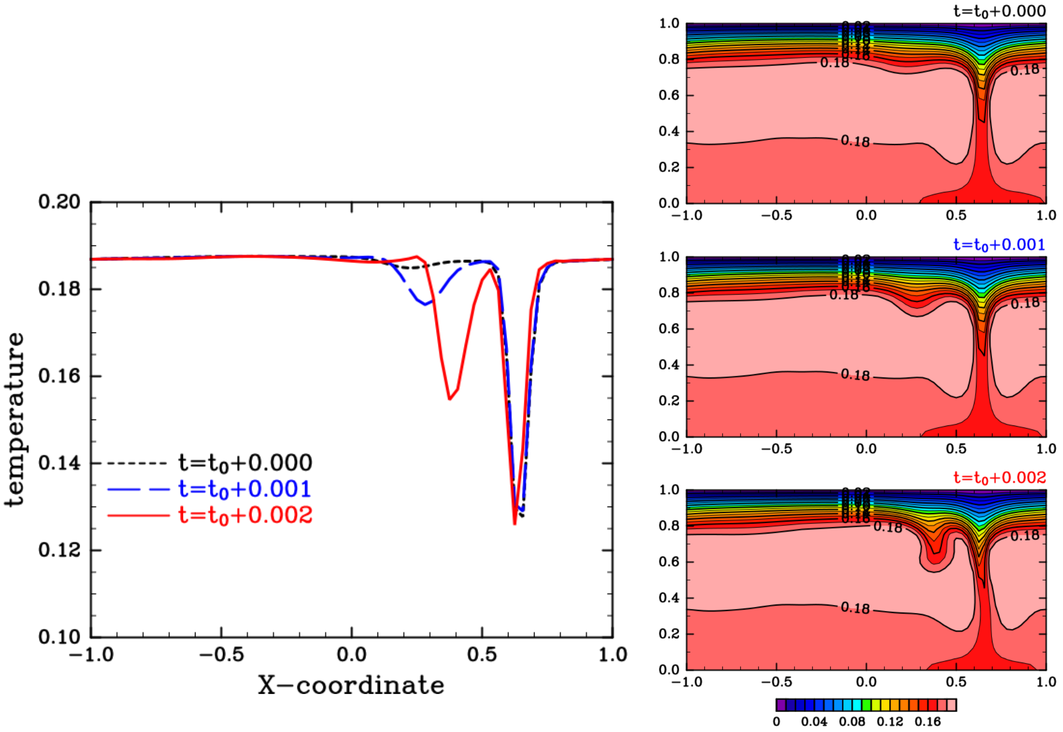

Figure 4.4: Snapshots of temperature distributions obtained by time integration for $Ra_0 = 1 \times 10^4$ and $\gamma = 40$. The left panel shows time evolution of temperature near the bottom of the boundary layer, at $y = 0.68$. t is dimensionless time, and t_0 is the time of plume growth initiation. Two cold plumes can be observed; the larger one corresponds to that of the steady solution and stays at $x = 0.6$. The smaller one grows due to the Rayleigh–Taylor instability and is carried from left to right by convective flow. The right panels show the evolution of temperature for the same time sequence as in the left panel.

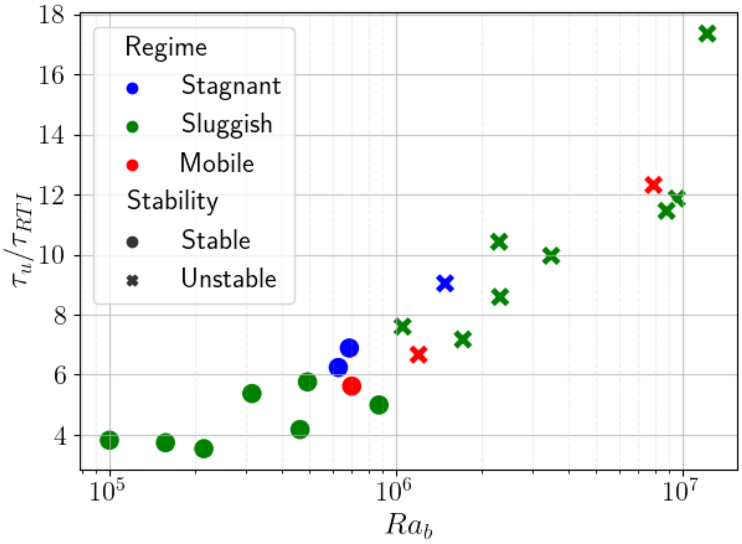

Figure 4.5: Results of time-dependent calculations on a diagram of Ra_b and a ratio of time scales of horizontal entrainment to the Rayleigh–Taylor instability. Circles and crosses denote stable and unstable solutions, respectively.

plume grows in the boundary layer and is carried by the convective flow to the location of the cold strong plume. Previous numerical models have found a similar behavior in which newly formed plumes are carried away by the horizontal flow generated by existing plumes. Merging of plumes leads to irregular patterns (e.g. Travis and Olson, 1994; Kameyama and Ogawa, 2000). Following these observations, we assume that the border between stability and instability is set by the relative speed of two processes: growth of a boundary layer instability and its entrainment by the preexisting convective flow. The mechanism for the growth of a plume instability in the boundary layer is explained by the Rayleigh–Taylor instability (e.g. Ribe, 2018), which can be used to determine the growth rate of plumes. The time scale for the entrainment is set by the horizontal velocity of the steady solution.

Figure 4.5 compares two time scales for the time integration solutions, and presents their importance for stability. The vertical axis, $\tau_u/\tau_{\mathrm{RTI}}$, represents a ratio of time scales: the time scale of horizontal entrainment by convective flow τ_u, and the growth time scale of a Rayleigh–Taylor instability at the boundary layer between the isothermal core and the conductive lid τ_{RTI}. They are obtained by the following equations:

$$\tau_u = \frac{\lambda}{2u}, \quad \tau_{\mathrm{RTI}} = \left[Ra_b r_{\eta\mathrm{eff}}^{-1} \delta \Delta T_{\mathrm{eff}} f\left(r_{\eta\mathrm{eff}}, 2\pi\delta/\lambda\right)\right]^{-1}. \tag{4.2}$$

Here, ΔT_{eff} is temperature difference across the active boundary layer, which is associated to $r_{\eta\mathrm{eff}}$ as $r_{\eta\mathrm{eff}} = \exp(\gamma \Delta T_{\mathrm{eff}})$. $f(r_{\eta\mathrm{eff}}, 2\pi\delta/\lambda)$ is the dimensionless growth rate of the Rayleigh–Taylor instability derived by Whitehead and Luther (1975) (their eq. A15), based on a linear stability analysis of an interface between a fluid layer and a fluid in an infinite half-space with different density and viscosity. The function f is expressed in terms of two arguments with simple notations: the viscosity contrast r and the horizontal wavenumber k,

$$f(r,k) = \frac{r}{2k}\left(\frac{r\left(\cosh(2k)-1\right)+\sinh(2k)-2k}{r^2\left(\sinh(2k)+2k\right)+2r\cosh(2k)+\sinh(2k)-2k}\right). \tag{4.3}$$

The other factors in τ_{RTI} of eq. (4.2) account for the translation to the dimensionless time scale from that in Whitehead and Luther (1975). The growth rate τ_{RTI} is evaluated by substituting the values of $r_{\eta\mathrm{eff}}$, δ, and λ obtained from our convective solutions to the function f.

From Figure 4.5, it can be understood that the stability of the steady solutions is determined by the ratio between the growing time scale of the Rayleigh–Taylor instability and the horizontal entrainment speed. The stable and unstable solutions are divided at $\tau_u/\tau_{\mathrm{RTI}} \approx 6.67$. Note that the stability of the solutions does not depend on their regime. Therefore, sluggish lid regime solutions whose time scale ratio is estimated less than the threshold can exist stably, even if they have large viscosity contrast across the boundary layer. Moreover, there are steady solutions with a thin strong downward plume and broad slow upward flow (Section 4.1) between $10^5 < Ra_b < 10^6$ in the mobile regime.

4.3 Effect of the boundary condition of the top surface

In Section 3.4, we found that the solutions in the sluggish lid regime have larger viscosity contrast across the active convective region $r_{\eta\mathrm{eff}}$ than that of the solutions in the stagnant lid or mobile regimes. During the sluggish lid regime, the top surface mobility changes drastically between fully mobile to motionless. In order to investigate the cause of large $r_{\eta\mathrm{eff}}$ during the change of mobility, we consider a totally motionless condition on the top surface and compare it to the initial problem in this section.

We performed steady-state calculations with a rigid boundary condition on the top surface instead of the stress-free condition. The top surface boundary condition (2.5) is replaced by

$$T = \psi = \frac{\partial \psi}{\partial y} = 0, \quad \text{at } y = 1. \tag{4.4}$$

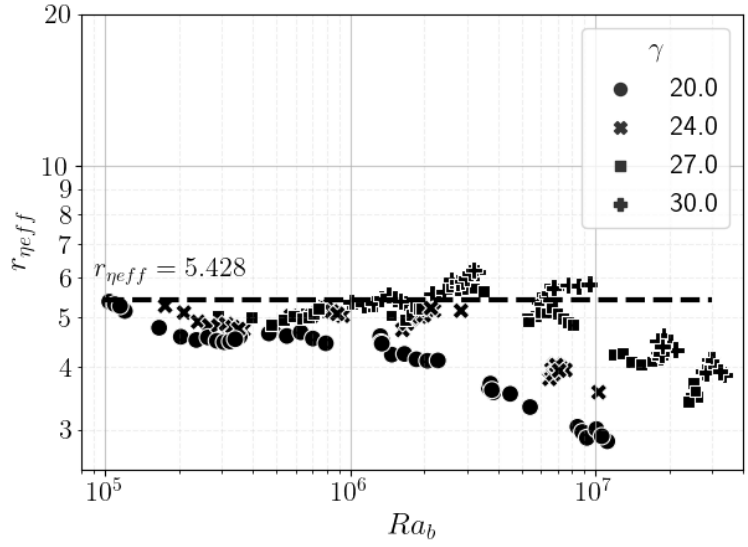

Figure 4.6: A plot of viscosity contrast $r_{\eta\mathrm{eff}}$ as a function of the Rayleigh number Ra_b for steady solutions with the rigid top boundary condition. The dashed line shows constant $r_{\eta\mathrm{eff}}$, which is the same as in Figure 3.8.

Using other governing equations and the same calculation method as described in Chapter 2, 156 solutions are obtained for this problem. Parameters are taken in the range of $1 \times 10 \leq Ra_0 \leq 1 \times 10^6$ and $\gamma = 20, 24, 27$, and 30, by which the parameter range of all regimes are covered for the stress-free problem.

Figure 4.6 shows the Ra_b–$r_{\eta\mathrm{eff}}$ diagram for the steady solutions with the rigid top boundary condition. The regimes of the solutions cannot be distinguished by the mobility criterion used above, because the horizontal flow vanishes at the top surface. To compare with Figure 3.8 for the stress-free condition, the same dashed line with constant value of $r_{\eta\mathrm{eff}}$ for the stagnant lid regime is overlaid. From Figure 4.6, $r_{\eta\mathrm{eff}}$ is almost constant or smaller than the constant value depending on Ra_b. However, no 'high $r_{\eta\mathrm{eff}}$' solution is found for solutions of the rigid top surface.

To clarify the situation further, we examine the behavior of the horizontally averaged bottom temperature T_b, the horizontally averaged temperature at the top of the active boundary layer T_l, and their difference $\Delta T_{\mathrm{eff}} = T_b - T_l$. Figure 4.7 shows the dependence of the temperatures on Ra_0 for the solutions of $\gamma = 27$ with different boundary conditions. In the left panel with the stress-free top boundary, the steep T_b curve in the sluggish lid regime appears due to the large difference in the scaling of T_b in the stagnant lid regime and the mobile lid regime. The T_l curve of the stagnant lid regime is almost parallel to the T_b curve, resulting in a constant ΔT_{eff}, which is consistent with the findings of previous studies (e.g. Davaille and Jaupart, 1993; Grasset and Parmentier, 1998). Since T_l in the mobile regime is close

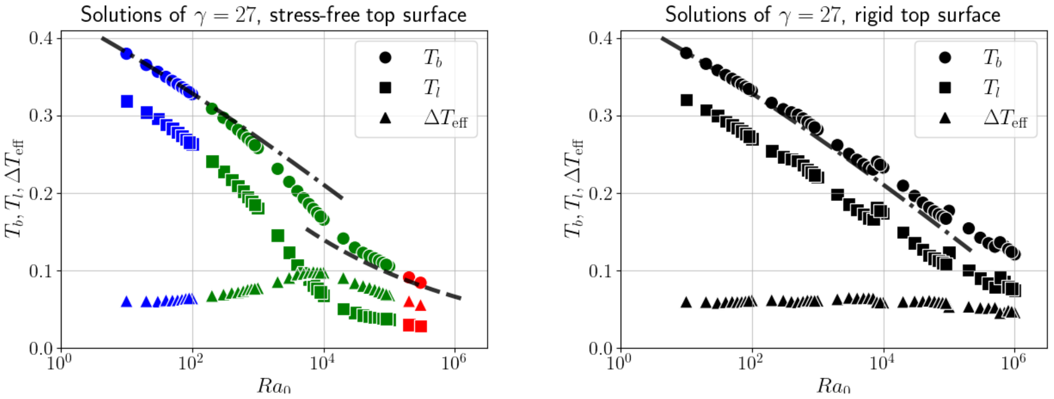

Figure 4.7: Dependencies of T_b (circles), T_l (squares), and $\Delta T_{\mathrm{eff}} = T_b - T_l$ (triangles) on Ra_0 are shown for the solutions of $\gamma = 27$. The cases with a stress-free top surface (left panel) and a rigid top surface (right panel) are shown. Dash-dotted lines are the scaling function for the stagnant lid regime (eq. 3.6) and a dashed line is that for the mobile regime (eq. 3.5). The color code on the left panel is the same as in the previous figures.

to 0 by definition, the T_l curve in the sluggish regime in a range $10^3 \lesssim Ra_0 \lesssim 10^4$ is steeper than that of T_b, in order to reach ≈ 0 for $Ra_0 \gtrsim 10^4$. Then ΔT_{eff} becomes larger than those of the stagnant lid regime and the mobile regime, resulting in the prominent profile of $r_{\eta\mathrm{eff}}$ shown in Figure 3.8. On the other hand, on the right panel for the case of the rigid condition, a single scaling of T_b as a function of Ra_0 seems to be applied over the entire range. Moreover, the T_l curve is smooth and almost parallel to the T_b curve. As a result, ΔT_{eff} is almost constant, resulting in the $r_{\eta\mathrm{eff}}$ plot without protrusion (Figure 4.6).

The comparison of the solutions between the different top dynamical boundary conditions elucidates that the prominent $r_{\eta\mathrm{eff}}$ in the sluggish lid regime is due to the differences in the scaling relationship of T_b between the stagnant lid regime and the mobile regime. In the case of the stress-free upper boundary condition, the convective motion is affected by the stress-free condition in the mobile regime, where no lid emerges. In the stagnant lid regime, the upper boundary of the active convective layer is adjacent to the conductive lid without motion, meaning that the effective dynamical condition is close to the rigid one. Therefore, the large discrepancy of the scaling relations between the stagnant lid regime and the mobile regime can be attributed to the effective upper boundary condition. In contrast, when the rigid condition is applied at the upper surface, the effective upper boundary condition for the active convective motion would not change drastically along the evolution of the conductive lid.

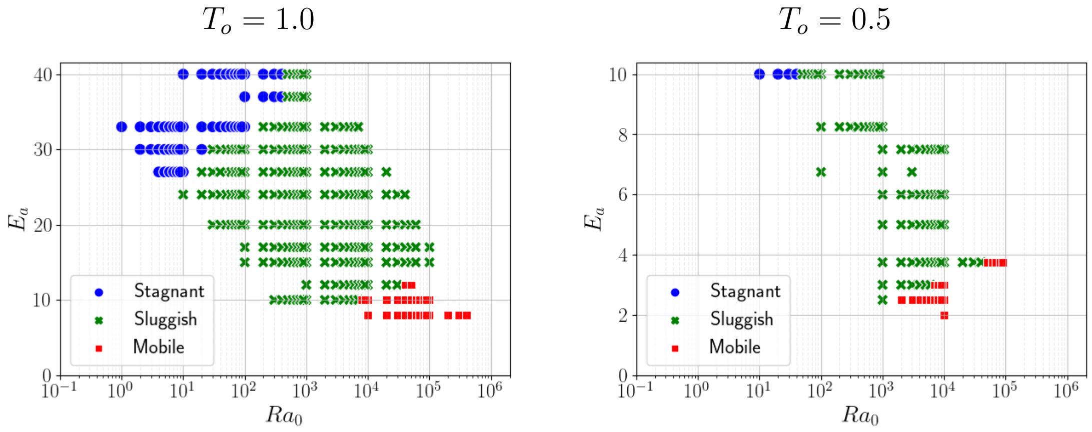

Figure 4.8: Steady solutions with Arrhenius viscosity on Ra_0–E_a diagram. Left and right panels are for $T_o = 1.0$ and $T_o = 0.5$, respectively. Colors indicate the regimes of the solutions, meaning of which are the same as those in Figure 3.1. The regime classification is based on mobility described in Section 3.1.

4.4 Comparison to model of the Arrhenius viscosity

We have adopted the Frank-Kamenetskii (FK) approximation viscosity (eq. 1.2) for the internal heating convection problem discussed so far, because it has been widely used for many numerical studies as a fundamental rheological model of mantle convection. However, it is useful to see the effects of different rheological models for applications to planetary problems. Here, we briefly perform numerical calculations of internal heating convection with the Arrhenius law viscosity (eq. 1.1) and compare their results with those with the FK approximation viscosity.

The dimensionless form of the Arrhenius-law viscosity is given by (e.g. Grigné, 2023)

$$\eta(T) = \exp\left[E_a\left(\frac{1}{T+T_o} - \frac{1}{T_o}\right)\right] = \exp\left[\frac{-E_a T}{T_o(T+T_o)}\right], \tag{4.5}$$

where E_a is dimensionless activation energy and T_o is temperature offset. T_o is usually selected as the absolute temperature at the reference location. The variable corresponding to the FK parameter γ in eq. (2.4) can be written as

$$\gamma_A(T) = \frac{E_a}{T_o\,(T+T_o)}. \tag{4.6}$$

The FK approximation assumes that γ is independent of temperature while γ_A depends on the absolute temperature $T + T_o$.

We seek steady solutions with the Arrhenius viscosity (4.5) instead of (2.4) for various values of E_a and Ra_0 using the Newton method described in Section 2.3.2.

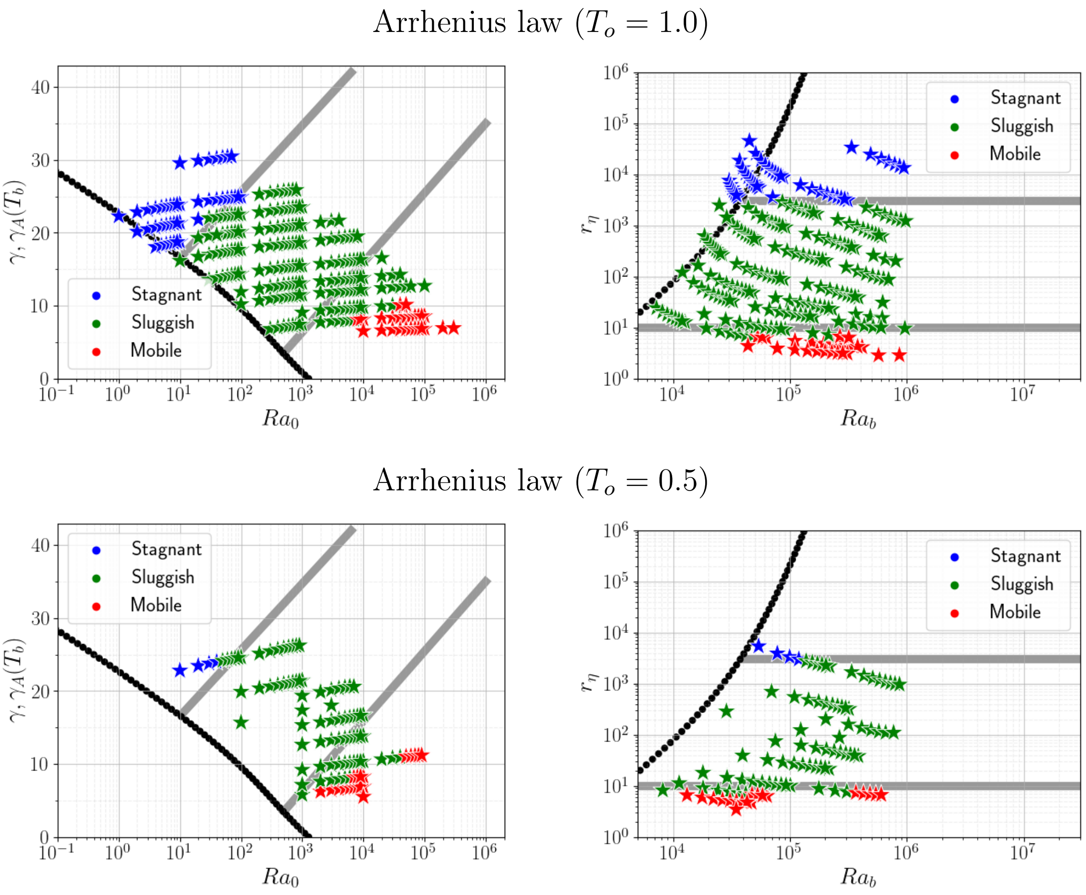
Arrhenius law ($T_o = 1.0$)

Arrhenius law ($T_o = 0.5$)

Figure 4.9: Regime diagrams for the Arrhenius viscosity solutions on the parameter planes with Ra_0–$\gamma_A(T_b)$ (left) and Ra_b–r_η (right). The colors of each solution indicate the regimes distinguished in the same way as described in section 3.1. Grey lines and black dots show the same regime boundaries and neutral values as those for the FK viscosity cases indicated in Figure 3.1, where γ is used in the vertical axis of the left panels instead of $\gamma_A(T_b)$. Upper and lower panels show the cases with $T_o = 1.0$ and $T_o = 0.5$, respectively.

The first estimate for the iterative calculation is given by a FK viscosity solution whose value of γ is equal to $\gamma_A(0)$. Two values of the temperature offset $T_o = 1.0$ and 0.5 are taken to evaluate the effect of the absolute temperature on the Arrhenius system. 240 solutions for $T_o = 1.0$ and 97 solutions for $T_0 = 0.5$ are successfully obtained. Figure 4.8 shows the steady solutions with their regime classification on the Ra_0–E_a diagram. It can be seen that even when the Arrhenius viscosity is applied to the internal heating convection problem, three different regimes are identified similar to the ones obtained with the FK viscosity law.

Figure 4.9 compares the regime diagrams of Arrhenius viscosity convection with those of FK viscosity convection shown in Figure 3.1. The values of $\gamma_A(T_b)$ are evaluated using T_b from the solutions of Arrhenius viscosity convection to project them to the $\gamma_A(T_b)$ axis of the left panel. We examine the consistency of the regime classification between Arrhenius viscosity convection and the FK viscosity convection. The same regime boundaries and neutral curve on each panel as shown in Figure 3.1 are represented by grey lines and black circles, while γ is used instead of $\gamma_A(T_b)$ on the vertical axis of the left panels. The regime boundaries with the Arrhenius law viscosity agree fairly well with that obtained for the FK viscosity, even though, for the mobile–sluggish lid boundary, it appears to be at a slightly lower value of $\gamma_A(T_b)$ (left panels). The agreement in the Ra_b–r_η space (right panels) seems to be even better than in the Ra_0–$\gamma_A(T_b)$ space.

We also investigate the effect of the temperature offset T_o, the additional parameter for the Arrhenius law viscosity. Comparing the diagrams for $T_o = 1.0$ (top panels) and $T_o = 0.5$ (bottom panels) of Figure 4.9, the sluggish lid–stagnant lid boundary is not influenced by the value of T_o in that range, while the change of the mobile–sluggish lid boundary is not clear, which should be examined further by obtaining more steady solutions. In addition, we should investigate the cases with smaller T_o, since the difference between the Arrhenius viscosity and the FK viscosity would become significant when $T_o < T$. Indeed, looking at eq. (4.6), we see that for $T \ll T_o$, $\gamma_A(T)$ tends to a constant value, similar to the FK viscosity law. Grigné (2023) showed that, in the case of bottom heating convection, different results are obtained for $T_o = 0.2$ and $T_o = 1$, a value often used in previous studies. The situation is rendered more complex in the case of internal heating where the temperature difference T_b decreases with the Rayleigh number. In our calculations, we typically have $T < T_o$, which limits the effects of the temperature offset of the Arrhenius law. More work will be needed to investigate this question systematically, in particular with lower values of $T_o < 0.5$.

Chapter 5

Conclusions

We have investigated the dynamical regimes of thermal convection in a temperature-dependent fluid driven by internal heating within a horizontal layer bounded by stress-free boundaries. Finite-amplitude steady solutions have been computed in a two-dimensional laterally periodic domain with an aspect ratio of 2, using the Newton method. We have obtained convective solutions in a wide range of the parameter set of the Rayleigh number defined using the top surface viscosity Ra_0, and the strength of temperature dependence of viscosity γ.

By classifying the steady solutions according to the top surface mobility M, we identify the sluggish lid regime in an intermediate range of the viscosity contrast between the mobile and stagnant lid regimes. The convection structure of the sluggish lid regime is characterized by two features: (i) the height of the convective region increases with the increase of Ra_0 while Ra_b, the Rayleigh number defined using the bottom viscosity, remains nearly constant, (ii) the viscosity contrast within the convective region is larger than the other regimes, whereas it is nearly constant in the stagnant lid regime and small in the mobile regime. When the stress-free boundary condition of the top surface is replaced by a rigid one, no solution with the large viscosity contrast is observed. This result suggests that the sluggish lid regime is caused by the change in the effective dynamical boundary condition at the top of the convective region. In the case of stress-free boundary condition, temperature at the top of the convective region T_l and that in the interior T_b depend on the Rayleigh number Ra_b differently due to the transition of the effective boundary condition between the mobile and stagnant lid regimes, which makes the prominent of temperature difference in the sluggish lid regime.

We have derived scaling relations for the Nusselt number as functions of the Rayleigh number defined using the bottom viscosity for the steady solutions in the mobile regime and the stagnant lid regime. The scaling law for the mobile regime at moderate Rayleigh numbers ($Ra_b \lesssim 10^5$) is obtained as $Nu \sim Ra_b^{1/4}$, which agrees with that of Grasset and Parmentier (1998). However, a different scaling law with a lower exponent, $Nu \sim Ra_b^{1/6}$, is obtained for high Rayleigh number solutions in both regimes ($Ra_b \gtrsim 10^5$). Our theoretical derivation of scaling relations shows that the 1/4 power law is originated from an assumption of a symmetric shape of convection cells, whereas the 1/6 power law is derived from an asymmetric structure of steady convection with high Rayleigh numbers that is dominated by a strong thin downward plume for each convection cell. Note that the scaling relations proposed by Grasset and Parmentier (1998) were examined by time-dependent simulations, in which the width of convection cells varied with time.

We have investigated the stability of steady solutions through time integration calculations. Thanks to the Newton method, we have succeeded in obtaining both stable and unstable steady solutions across all the regimes. The stability threshold locates at $Ra_b \approx 10^6$. The results of stability is consistent with the theoretical examination of the Rayleigh-Taylor instability, where the timescales for plume growth and entrainment by the background convective flow are compared quantitatively. Some cases of sluggish lid convection remain stable in time-dependent systems, even though a large viscosity contrast arises across the boundary layer.

Finally, we have briefly examined steady solutions of internally heated convection with the Arrhenius-law viscosity. As in the case of the Frank-Kamenetskii (FK) approximation, three regimes are identified using the same method of the regime classification. By converting the Arrhenius viscosity parameters into the FK viscosity parameter, the regime diagrams obtained for the Arrhenius viscosity solutions are qualitatively consistent with the regime diagram for the FK viscosity solutions. There is a slight discrepancy in the location of the regime boundary between the mobile and sluggish lid regimes. This discrepancy may depend on the absolute temperature, which is an additional parameter for the Arrhenius viscosity. It is expected that the results obtained with the FK approximation would be useful for extending the Arrhenius viscosity convection problem and perhaps other problems involving more complex viscosity.

Different convective structures are successfully observed depending on parameters in this study. By the analyses of these structures, the convective regimes, distinguished by the surface mobility, are confirmed to be reflected in the different scaling behaviors among three regimes as well as shown in other convection problems with temperature-dependent viscosity. It is indicated that thermal convection problems with temperature-dependent viscosity exhibit essentially different patterns in their solutions, even though a simple function with only one parameter for viscosity is applied.

From the geophysical perspective, the regime diagrams obtained in this study will serve fundamental insights into the interior structures of terrestrial planets, which are closely related to their dynamical states and surface environments. For example, the sluggish lid and stagnant lid regimes are considered to correspond to the drifting and motionless plates covering the Earth's surface (Bercovici et al., 2000). As sluggish lid convection exhibits the dynamical coupling of mantle convection and plate tectonics, this study will help understand the essential mechanism underlying the formation of drifting and stagnant lids, even though more realistic models of the mantle rheology will be required to reproduce Earth-like behaviors.

This study may also be useful to deduce the evolution of interior structures over thermal histories of terrestrial planets. During the evolution of terrestrial planets, they are expected to follow a path in a parameter space of heat flow and thermal states, which is constrained by scaling laws associated with the convective regimes (e.g. Sleep, 2000). The regimes usually considered are the magma ocean, plate tectonic, and non-plate-tectonic states, which correspond respectively to the mobile, sluggish lid, and stagnant lid regimes. The latter two states are currently applied to the present-day terrestrial planets in the Solar System. Transitions between regimes may occur back and forth, leading to episodicity (Fowler and O'Brien, 1996; Sleep, 2000). If a planet is far from the conditions for the plate tectonics to arise, the relevant regimes can include all of the mobile, sluggish lid, and stagnant lid regimes, covering both the past and future states. By using the regime diagram obtained in this study and a one-dimensional thermal evolution model, we can predict the styles of mantle convection throughout the evolution, tracking the transitions of parameters of the convection problem over the planetary time scale. Moreover, it may be possible to estimate the interior states of terrestrial exoplanets from observations of their surfaces realized in the future.

Based on the present study, we should investigate the effect of the horizontal length scale of convection on the scaling relations and the regime classification. The aspect ratio may influence the emergence of asymmetric convection cells described in Section 4.1. For bottom-heated convection, the aspect ratio affects the scaling relations (Okuda and Takehiro, 2023), which showed horizontally elongated solutions are preferred in the sluggish lid regime. Horizontally extended convection has also been observed in time-dependent models driven by internal heating (Vilella and Deschamps, 2017) and secular cooling (Morison et al., 2021). A systematic investigation of aspect ratio dependence could provide a further insight into the formation of convective patterns.

Moreover, for geophysical application, the present results should be extended to three-dimensional spherical geometries and realistic rheological models. For example, Javaheri et al. (2024) suggests that the spherical geometry has a significant effect on the regime boundaries for bottom-heated convection. Our brief investigation for Arrhenius viscosity convection has suggested slight shifts in regime boundaries depending on the additional parameters. Since Grigné (2023) also suggested that the absolute temperature affects the emergence of solutions in the stagnant lid and sluggish lid regimes, the characteristics of the solutions in each regime should be examined. Looking toward further development to the geophysical and planetary sciences, thermal convection problems with stress-dependent rheology may exhibit the plate-tectonic behavior (e.g. Ogawa, 2003), and thermal convection involving compressibility may also become important in the context of the super-Earth (Ricard et al., 2022). The mathematical analyses will help understand these complex systems.

Appendix A

A.1 Linear stability problem of hydrostatic state

The linear stability analysis of the hydrostatic state is performed to specify a range of controlled parameter sets (Ra_0, γ) in which convection is expected to occur. We follow a classical approach (e.g. Chandrasekhar, 1961; Stengel et al., 1982; Labrosse et al., 2018). The hydrostatic state of the governing equations (2.2)–(2.7) is

$$T_0 = \frac{1 - y^2}{2}, \quad \psi_0 = 0. \tag{A.1}$$

Linearized equations of infinitesimal perturbations θ, ψ from the static state (A.1) are derived substituting $T_0 + \theta$ and ψ to the nonlinear governing equations and omitting higher order terms:

$$\frac{\partial \theta}{\partial t} = y \frac{\partial \psi}{\partial x} + \nabla^2 \theta, \tag{A.2}$$

$$\left(\frac{\partial^2}{\partial x^2} - \frac{\partial^2}{\partial y^2} \right) \left[\eta(T_0) \left(\frac{\partial^2}{\partial x^2} - \frac{\partial^2}{\partial y^2} \right) \psi \right] + 4 \frac{\partial^2}{\partial x \partial y} \left(\eta(T_0) \frac{\partial^2 \psi}{\partial x \partial y} \right) = -Ra_0 \frac{\partial \theta}{\partial x}, \tag{A.3}$$

$$\theta(y = 1) = \frac{\partial \theta}{\partial y}(y = 0) = \psi(y = 0, 1) = \frac{\partial^2 \psi}{\partial y^2}(y = 0, 1) = 0. \tag{A.4}$$

We assume that the perturbations θ and ψ are written as the product of a function of the vertical coordinate $\theta(y), \psi(y)$, a harmonic function of the horizontal coordinate $\exp(2\pi i x/\lambda)$, and an exponential time evolution function $\exp(\sigma t)$, where σ is a growth rate of perturbations. Substituting them in the linearized equations (A.2)–(A.4), and using first and second order derivatives of η by y

$$\frac{\mathrm{d}\eta}{\mathrm{d}y} = \gamma y \eta(T_0) + \mathcal{O}(\theta), \quad \frac{\mathrm{d}^2\eta}{\mathrm{d}y^2} = \left(\gamma + \gamma^2 y^2 \right) \eta(T_0) + \mathcal{O}(\theta), \tag{A.5}$$

the ordinary differential equations are obtained:

$$0 = -\frac{2\pi}{\lambda} y\psi + \left(\frac{\mathrm{d}^2}{\mathrm{d}y^2} - k^2 - s \right) \theta, \tag{A.6}$$

$$\begin{aligned} Ra_0\theta = -\eta(T_0)\frac{\lambda}{2\pi} \Bigg[& \frac{\mathrm{d}^4}{\mathrm{d}y^4} + 2\gamma y \frac{\mathrm{d}^3}{\mathrm{d}y^3} + \left(\gamma + \gamma^2 y^2 - 2k^2\right) \frac{\mathrm{d}^2}{\mathrm{d}y^2} \\ & - 2\gamma y k^2 \frac{\mathrm{d}}{\mathrm{d}y} + k^2 \left(\gamma + \gamma^2 y^2 + k^2\right) \Bigg] \psi, \end{aligned} \tag{A.7}$$

$$\theta(y=1) = \frac{\partial \theta}{\partial y}(y=0) = \psi(y=0,1) = \frac{\partial^2 \psi}{\partial y^2}(y=0,1) = 0. \tag{A.8}$$

These equations describes an eigenvalue-eigenfunction problem. The neutral stability with horizontal wavelength of 2 is obtained solving this problem with $\sigma = 0$, $\lambda = 2$, and each fixed value of γ. The lowest eigenvalue that gives a non-trivial eigenfunction is selected to give the neutral stability of each setting of γ. The neutral values are thus written as $Ra_{0n}(\gamma)$. We calculate $Ra_{0n}(\gamma)$ using a finite difference method, varying the value of γ from 0 to 40. This results are plotted in Figure 3.1.

Acknowledgement

I would like to extend my sincere gratitude to all those who have supported me during my PhD studies.

First, I would like to express my appreciation to my supervisor, Prof. Shin-ichi Takehiro, for his invaluable insights into fluid dynamics and geophysics, as well as for his guidance on both numerical and theoretical research techniques. His practical and philosophical advice, along with his heartfelt encouragement, has greatly supported me throughout my graduate studies.

I would also like to express my appreciation to Prof. Stéphane Labrosse, who kindly hosted me at the École Normale Supérieure de Lyon (ENS de Lyon) and provided invaluable advice that made it possible for me to complete this study. The experience I gained under his supervision has greatly broadened my academic perspective.

I would also like to thank the current and former members of the fluid dynamics research group at the Research Institute for Mathematical Sciences (RIMS), Kyoto University. I am particularly grateful to Prof. Yamada, Prof. Ohkitani, Prof. Ishimoto, Dr. Yasuda, Dr. Hiruta, and Mr. Ogawa for stimulating and fruitful discussions and suggestions from various aspects of fluid dynamics and computation.

My graduate studies have been supported by RIMS providing me with a great research environment. This study has also been supported financially by the SPRING program (Grant No. JPMJSP2110) from the Japan Science and Technology Agency. The Graduate School of Mathematics and Mathematical Sciences at Kyoto University supported my visit to ENS de Lyon through the programs of the Super Global Course and the Mathematics and Mathematical Sciences Innovation Course.

The numerical calculations in this work were performed on the computer systems of RIMS. The 'Gtool5' library (Ishiwatari et al., 2012) was used for the input and output of numerical data. The products of the Dennou-Ruby project (https://www.gfd-dennou.org/arch/ruby/) were used for data visualization.

Finally, I am deeply grateful to my family for their constant support and understanding, and to my friends for their companionship and encouragement.

References

D. J. Andrews. Numerical simulation of sea-floor spreading. J. Geophys. Res., 77(32): 6470–6481, 1972. doi: 10.1029/JB077i032p06470.

H. Bénard. Les Tourbillons cellulaires dans une nappe liquide. Revue générale des Sciences pures et appliquées, 11(1261–1271), 1900.

D. Bercovici, Y. Ricard, and M. A. Richards. The relation between mantle dynamics and plate tectonics: A primer. In The History and Dynamics of Global Plate Motions, volume 121, pages 5–46. American Geophysical Union, 2000. doi: 10.1029/GM121p0005.

F. H. Busse. Non-stationary finite amplitude convection. J. Fluid Mech., 28(2):223–239, 1967a. doi: 10.1017/S0022112067002034.

F. H. Busse. On the stability of two-dimensional convection in a layer heated from below. J. Math. Phys., 46(1–4):140–150, 1967b. doi: 10.1002/sapm1967461140.

S. Chandrasekhar. Hydrodynamic and Hydromagnetic Stability. Oxford university press, 1961.

G. Choblet and C. Sotin. 3D thermal convection with variable viscosity: Can transient cooling be described by a quasi-static scaling law? Phys. Earth Planet. Inter., 119(3): 321–336, 2000. doi: 10.1016/S0031-9201(00)00136-9.

U. Christensen. Convection with pressure- and temperature-dependent non-Newtonian rheology. Geophys. J. R. Astr. Soc., 77(2):343–384, 1984. doi: 10.1111/j.1365-246X.1984.tb01939.x.

A. Davaille and C. Jaupart. Transient high-rayleigh-number thermal convection with large viscosity variations. J. Fluid Mech., 253:141–166, 1993. doi: 10.1017/S0022112093001740.

F. Deschamps, C. Yao, P. J. Tackley, and C. Sanchez-Valle. High Rayleigh number thermal convection in volumetrically heated spherical shells. J. Geophys. Res. Planets, 117(E9), 2012. doi: 10.1029/2012JE004090.

B. J. Foley and P. E. Driscoll. Whole planet coupling between climate, mantle, and core: Implications for rocky planet evolution. Geochem. Geophys. Geosyst., 17(5):1885–1914, 2016. doi: 10.1002/2015GC006210.

A. C. Fowler. Fast Thermoviscous Convection. Stud. App. Math., 72(3):189–219, 1985. doi: 10.1002/sapm1985723189.

A. C. Fowler and S. B. G. O'Brien. A mechanism for episodic subduction on Venus. J. Geophys. Res. Planets, 101(E2):4755–4763, 1996. doi: 10.1029/95JE03261.

O. Grasset and E. M. Parmentier. Thermal convection in a volumetrically heated, infinite Prandtl number fluid with strongly temperature-dependent viscosity: Implications for planetary thermal evolution. J. Geophys. Res. Solid Earth, 103(B8):18171–18181, 1998. doi: 10.1029/98JB01492.

C. Grigné. Stagnant-lid convection: comparison of viscosity laws and uniform scaling approach for temperature and heat flux prediction. Geophys. J. Int., 235(3):2410–2429, 2023. doi: 10.1093/gji/ggad375.

C. Hüttig and D. Breuer. Regime classification and planform scaling for internally heated mantle convection. Phys. Earth Planet. Inter., 186:111–124, 2011. doi: 10.1016/j.pepi.2011.03.011.

M. Ishiwatari, E. Toyoda, Y. Morikawa, S. Takehiro, Y. Sasaki, S. Nishizawa, M. Odaka, N. Otobe, Y. O. Takahashi, K. Nakajima, T. Horinouchi, M. Shiotani, Y.-Y. Hayashi, and Gtool development group. "Gtool5": a Fortran90 library of input/output interfaces for self-descriptive multi-dimensional numerical data. Geoscientific Model Development, 5(2):449–455, 2012. doi: 10.5194/gmd-5-449-2012.

C. Jain and V. S. Solomatov. Onset of convection in internally heated fluids with strongly temperature-dependent viscosity. Phys. Fluids, 34:096604, 2022. doi: 10.1063/5.0105170.

C. Jaupart, S. Labrosse, F. Lucazeau, and J.-C. Mareschal. 7.06 - Temperatures, Heat, and Energy in the Mantle of the Earth. In Treatise on Geophysics, pages 223–270. Elsevier, Oxford, Second edition, 2015. doi: 10.1016/B978-0-444-53802-4.00126-3.

P. Javaheri, J. P. Lowman, and P. J. Tackley. Spherical geometry convection in a fluid with an Arrhenius thermal viscosity dependence: The impact of core size and surface temperature on the scaling of stagnant-lid thickness and internal temperature. Phys. Earth Planet. Inter., 349:107157, 2024. doi: 10.1016/j.pepi.2024.107157.

M. Kameyama. 2-D numerical experiments of thermal convection of highly viscous fluids under strong adiabatic compression: implications on mantle convection of super-Earths with various sizes. Earth Planets Space, 77(13), 2025. doi: 10.1186/s40623-025-02134-8.

M. Kameyama and M. Ogawa. Transitions in thermal convection with strongly temperature-dependent viscosity in a wide box. Earth Planet. Sci. Lett., 180(3):355–367, 2000. doi: 10.1016/S0012-821X(00)00171-0.

S. Labrosse, A. Morison, R. Deguen, and T. Alboussière. Rayleigh-Bénard convection in a creeping solid with a phase change at either or both horizontal boundaries. J. Fluid Mech., 846:5–36, 2018. doi: 10.1017/jfm.2018.258.

D. P. McKenzie, J. M. Roberts, and N. O. Weiss. Convection in the earth's mantle: towards a numerical simulation. J. Fluid Mech., 62(3):465–538, 1974. doi: 10.1017/S0022112074000784.

L.-N. Moresi and V. S. Solomatov. Numerical investigation of 2D convection with extremely large viscosity variations. Phys. Fluids, 7(9):2154–2162, 09 1995. doi: 10.1063/1.868465.

A. Morison, S. Labrosse, and G. Choblet. Sublimation-driven convection in Sputnik Planitia on Pluto. Nature, 600:419–423, 2021. doi: 10.1038/s41586-021-04095-w.

S. Morris and D. Canright. A boundary-layer analysis of Benard convection in a fluid of strongly temperature-dependent viscosity. Phys. Earth Planet. Inter., 36(3):355–373, 1984. doi: 10.1016/0031-9201(84)90057-8.

M. Ogawa. Plate-like regime of a numerically modeled thermal convection in a fluid with temperature-, pressure-, and stress-history-dependent viscosity. J. Geophys. Res. Solid Earth, 108(B2), 2003. doi: 10.1029/2000JB000069.

H. Okuda and S. Takehiro. Horizontal length of finite-amplitude thermal convection cells with temperature-dependent viscosity. Phys. Earth Planet. Inter., 344:107103, 2023. doi: 10.1016/j.pepi.2023.107103.

H. Okuda, S. Takehiro, and S. Labrosse. Convective regimes of internally heated steady thermal convection of temperature-dependent viscous fluid. Phys. Earth Planet. Inter., 367:107415, 2025. doi: 10.1016/j.pepi.2025.107415.

E. M. Parmentier and C. Sotin. Three-dimensional numerical experiments on thermal convection in a very viscous fluid: Implications for the dynamics of a thermal boundary layer at high Rayleigh number. Phys. Fluids, 12(3):609–617, 2000. doi: 10.1063/1.870267.

E. M. Parmentier, C. Sotin, and B. J. Travis. Turbulent 3-D thermal convection in an infinite Prandtl number, volumetrically heated fluid: implications for mantle dynamics. Geophys. J. Int., 116(2):241–251, 02 1994. doi: 10.1111/j.1365-246X.1994.tb01795.x.

C. C. Reese, V. S. Solomatov, J. R. Baumgardner, and W.-S. Yang. Stagnant lid convection in a spherical shell. Phys. Earth Planet. Inter., 116(1):1–7, 1999. doi: 10.1016/S0031-9201(99)00115-6.

C. C. Reese, V. S. Solomatov, and J. R. Baumgardner. Scaling laws for time-dependent stagnant lid convection in a spherical shell. Phys. Earth Planet. Inter., 149(3):361–370, 2005. doi: 10.1016/j.pepi.2004.11.004.

N. M. Ribe. Theoretical Mantle Dynamics. Cambridge University Press, 2018. doi: 10.1017/9781316795897.

Y. Ricard. 7.02 - Physics of Mantle Convection. In Treatise on Geophysics, pages 23–71. Elsevier, Oxford, Second edition, 2015. doi: 10.1016/B978-0-444-53802-4.00127-5.

Y. Ricard, T. Alboussière, S. Labrosse, J. Curbelo, and F. Dubuffet. Fully compressible convection for planetary mantles. Geophys. J. Int., 230(2):932–956, 2022. doi: 10.1093/gji/ggac102.

P. H. Roberts. Convection in horizontal layers with internal heat generation. Theory. J. Fluid Mech., 30(1):33–49, 1967. doi: 10.1017/S0022112067001284.

G. Schubert, D. L. Turcotte, and P. Olson. Mantle Convection in the Earth and Planets. Cambridge University Press, 2001.

N. H. Sleep. Evolution of the mode of convection within terrestrial planets. J. Geophys. Res. Planets, 105(E7):17563–17578, 2000. doi: 10.1029/2000JE001240.

V. S. Solomatov. Scaling of temperature- and stress-dependent viscosity convection. Phys. Fluids, 7(2):266–274, 02 1995. doi: 10.1063/1.868624.

V. S. Solomatov and L.-N. Moresi. Scaling of time-dependent stagnant lid convection: Application to small-scale convection on Earth and other terrestrial planets. J. Geophys. Res. Solid Earth, 105(B9):21795–21817, 2000. doi: 10.1029/2000JB900197.

C. Sotin and S. Labrosse. Three-dimensional thermal convection in an iso-viscous, infinite Prandtl number fluid heated from within and from below: applications to the transfer of heat through planetary mantles. Phys. Earth Planet. Inter., 112(3):171–190, 1999. doi: 10.1016/S0031-9201(99)00004-7.

K. C. Stengel, D. S. Oliver, and J. R. Booker. Onset of convection in a variable-viscosity fluid. J. Fluid Mech., 120:411–431, 1982. doi: 10.1017/S0022112082002821.

P. J. Tackley. Self-consistent generation of tectonic plates in time-dependent, three-dimensional mantle convection simulations 2. Strain weakening and asthenosphere. Geochem. Geophys. Geosyst., 1(8), 2000. doi: 10.1029/2000GC000043.

M. Thiriet, D. Breuer, C. Michaut, and A.-C. Plesa. Scaling laws of convection for cooling planets in a stagnant lid regime. Phys. Earth Planet. Inter., 286:138–153, 2019. doi: 10.1016/j.pepi.2018.11.003.

B. Travis and P. Olson. Convection with internal heat sources and thermal turbulence in the Earth's mantle. Geophys. J. Int., 118(1):1–19, 1994. doi: 10.1111/j.1365-246X.1994.tb04671.x.

D. J. Tritton and M. N. Zarraga. Convection in horizontal layers with internal heat generation. experiments. J. Fluid Mech., 30(1):21–31, 1967. doi: 10.1017/S0022112067001272.

D. Turcotte and G. Schubert. Geodynamics. Cambridge University Press, Third edition, 2014.

K. Vilella and F. Deschamps. Thermal convection as a possible mechanism for the origin of polygonal structures on Pluto's surface. J. Geophys. Res., 122:1056–1076, 2017. doi: 10.1002/2016JE005215.

J. A. Whitehead and D. S. Luther. Dynamics of laboratory diapir and plume models. J. Geophys. Res., 80(5):705–717, 1975. doi: 10.1029/JB080i005p00705.